Flow structure around a vertical cylinder placed in an open channel under combined wave-current flows

Wen-Yi Chang[1] and George Constantinescu[2]
[1]*National Center for High-Performance Computing, National Applied Research Laboratories, Hsinchu 30076, Taiwan*
[2]*Department of Civil and Environmental Engineering & IIHR Hydroscience and Engineering, The University of Iowa, Iowa City City, Iowa 52240, USA*

(Received 5 June 2024; accepted 24 January 2025; published 20 February 2025)

A series of simulations with a circular cylinder of diameter D placed in an open channel flow of depth H are conducted in both purely oscillatory flow (one-mode forcing with maximum orbital velocity, U_m) and in combined oscillatory and current flow regime (mean velocity, U_s). The paper discusses how the phase-averaged flow, the coherent structures generated around the cylinder, and the forces induced on the cylinder change with the ratio between the steady current velocity and the oscillatory velocity ($0 \leqslant U_s/U_m \leqslant 1.4$) and with the Keulegan-Carpenter number, $\mathrm{KC} = U_m T/D$ ($1.5 \leqslant \mathrm{KC} \leqslant 30.8$), where T is the period of the oscillatory flow. Results show that for constant U_s/U_m, the capacity of the horseshoe vortex to erode the bed increases with the KC number. For constant KC number, the overall coherence and lifespan of the main horseshoe vortex forming during each oscillatory cycle increase with U_s/U_m. The same is true for the number and initial circulation of the wake vortices shed on the downstream side of the cylinder in the simulations conducted with KC = 15.4 and 30.8. An instability in the form of large-scale hairpin-like vortices develops along the vertical cores of the wake vortices in the KC = 1.5 simulations with $U_s/U_m \geqslant 1.0$. For combined wave-current flows with $U_s/U_m \geqslant 0.4$, the regions of relatively high bed shear stress magnitude and the peak values inside these regions increase monotonically with the KC number for constant U_s/U_m. Results show that even for cases with a steady current, the oscillatory component of the phase-averaged in-line force is reasonably well described by Morisson's equation. A drag coefficient can be defined for the steady component of the in-line force with U_s as the velocity scale. For high KC numbers and $U_s/U_m > 1$ this drag coefficient is comparable to the standard drag coefficient in steady flow. The phase lag between the in-line force and the oscillatory velocity component decreases with increasing KC and is independent of U_s/U_m. For cases where the number of vortices shed in the wake is the same during all cycles, the phase-averaged spanwise force remains small. However, at times, the cylinder is subject to instantaneous forces of comparable magnitude along the streamwise and spanwise directions for KC $\geqslant$ 15.4, which has important consequences for the design of piles in combined wave-current flow.

DOI: 10.1103/PhysRevFluids.10.024804

I. INTRODUCTION

Sediment transport and the associated scour occurring around the base of piles and piers in estuaries, coastal and marine environments is due to the combined action of waves and currents. To correctly design the foundation of monopiles supporting offshore wind turbines and/or to decide on the proper sizing for riprap stone protecting the piles one needs to be able to accurately estimate the maximum bed shear stresses, the size and position of the regions of high bed shear stress around the base of the pile, and the erosive capability of the flow around the pile for a range of flow conditions

[1]. Such flow conditions can be quite complex due to the presence of tidal motions and waves that are superimposed on quasisteady currents. In some applications, one is interested to quantify the forces acting on such structures for both strength and fatigue analysis. The present study tries to contribute to the general understanding of the physics of such flows by focusing on the canonical case of an isolated, surface-piercing, vertical, circular cylinder placed in an open channel with a horizontal bed. The study relies on eddy-resolving simulations to investigate the critical role played by large-scale coherent structures generated by the interaction of the flow with the cylinder. The combined wave-current flow consists of a unimodal oscillatory flow component superimposed on a steady-current component.

The dynamics of the coherent structures driving scour around the upstream face (e.g., horseshoe vortex system containing a main vortex undergoing bimodal oscillations) and in the wake (e.g., vortex tubes and billow or lee-wake vortices that are stretched as they interact with the channel bed) of a circular cylinder placed in a steady, high-Reynolds-number current is well understood (e.g., see [2–16]). Some of these studies also provide information of the Strouhal number associated with the shedding of wake billows and the drag forces acting on the cylinder.

The other limiting case of a cylinder placed in a purely oscillatory/wave flow has also been the object of experimental and numerical investigations (e.g., [5,17–19]). Another category of relevant investigations, starting with the pioneering study conducted by [20], considered the case of a long cylinder parallel to the free surface [21–26]. The main information provided by these studies of flow past a long, horizontal cylinder in oscillatory flow was the number of shed wake vortices in each oscillatory cycle and the temporal variation of the forces acting on the cylinder. These results are also directly applicable to cases when a vertical, surface-piercing cylinder is mounted on a horizontal surface. In particular, these studies showed that the number of shed vortices in each oscillatory cycle is mainly a function of the Keulegan-Carpenter number, $\mathrm{KC} = U_m T/D$, where T is the period of the oscillatory flow, U_m is the maximum streamwise velocity away from the cylinder, and D is the cylinder diameter. For vertical cylinders placed on a horizontal bed [19], discusses the dynamics of the horseshoe vortex system and the variation of the bed shear stress distributions over the oscillatory cycle. Their study focused on determining how the lifespan of the horseshoe vortex during each oscillatory cycle and the distance from the cylinder at which the incoming boundary layer separates vary with the KC number.

In the case of a vertical, surface-mounted cylinder placed in oscillatory flow, a minimum value of the KC number is needed for horseshoe vortices to form every half cycle and for vertical vortices to be shed in the wake (e.g., see [17,19]). Horseshoe vortices are not present over the full oscillatory cycle. Meanwhile, the bottom parts of the vertical billow vortices undergo little stretching inside the bottom boundary layer, which explains their increased capacity to entrain sediment in oscillatory flow compared to steady current flow. A recent study [17] showed that a third type of coherent structures in the form of horizontal, near-bed vortices contributes to increasing the sediment erosive potential of the flow in the wake of a cylinder placed in oscillatory flow. The same study showed that the in-line (streamwise drag), phase-averaged force variation over an oscillatory cycle is well approximated by Morrison's equation that assumes the total streamwise force can be decomposed into a drag component and an inertial component [27]. Another main finding of [17] was that the surface-mounted cylinder is subject to nonzero phase-averaged spanwise drag forces over a range of KC numbers. Even for very low, or for very high, KC numbers, when the phase-averaged spanwise force is equal to zero, the cylinder can still be subject to large instantaneous spanwise forces during some of the oscillatory cycles.

Though the case of a vertical pile placed in a combined wave-current flow made the object of numerous investigations (e.g., [1,19,28–42]), most of these studies focused on predicting the scour evolution and the equilibrium scour bathymetry around the pile and on investigating the efficiency of different scour protection measures (e.g., rock armor). For combined wave-current flow cases, besides the KC number, the flow structure is controlled by the ratio of the steady current velocity to the oscillatory velocity, $U_s' = U_s/U_m$, or, equivalently, by the combined wave-current parameter, $U_s/(U_s + U_m)$. Much less attention was paid to investigating the physics of these flows and, in particular, the dynamics of the large-scale coherent structures generated around the cylinder with varying KC number and U_s'. The main result was reported by [19] who found that the overall effect of the steady flow component was to increase the lifetime of the horseshoe vortex over each oscillatory cycle and the separation distance of the incoming boundary layer. Unfortunately, no information is available on how the presence of a steady flow component affects the number of shed vortices and the dynamics of these vortices once they move away from the cylinder. Such information is critical given that for flows with a strong oscillatory component the wake vortices are characterized by a large erosive potential.

Experimental investigations that can provide a detailed description of the dynamics of these eddies and their interaction with the bed surface requires the use of 2D or 3D particle image velocimetry. Unfortunately, such studies are not available for cylinders in combined wave-current flows. Though unsteady Reynolds-averaged Navier-Stokes (URANS) simulations were found to predict fairly well the bed evolution and main flow features in steady and unsteady flow around surface-mounted cylinders (e.g., see [5,37]), this approach has also some important limitations related to its capability to capture the dynamics of larger-scale eddies generated by the interaction of the approaching flow with a surface-mounted cylinder. For example, URANS simulations do not capture the formation of vortex tubes in the separated shear layers, while the dynamics and coherence of the wake billow vortices is not predicted very accurately. Moreover, such simulations cannot capture the bimodal oscillations of the horseshoe vortices forming in steady current cases [10,43] and underpredict the bed shear stress amplification beneath the horseshoe vortex system in oscillatory flow cases [44].

Due to the huge computational resources needed, direct numerical simulations (DNS) of such flows are limited to very low Reynolds numbers where the dynamics of the wake vortices and of the horseshoe vortices is very different to that of interest for practical applications related to monopiles present in marine and coastal environments. Most attempts to perform DNS (e.g., [25]) were limited to 2D simulations of purely oscillatory cases (no bed was present) at very low Reynolds numbers (e.g., cylinder Reynolds number defined with the maximum approaching flow velocity, Re_m, of less than 2000). For the same reasons, 3D DNS was limited not only to small Reynolds numbers (e.g., less than 1000) but also to small KC numbers (e.g., see [45]). On the other hand, eddy-resolving numerical simulations based on the large eddy simulation (LES) approach can accurately capture the physics of the coherent structures generated around surface-mounted cylinders at sufficiently high Reynolds numbers (e.g., $\mathrm{Re}_m > 10^4$) and are computationally much less expensive compared to DNS.

The present study uses the same eddy-resolving numerical model as the one employed by [17] to investigate flow and turbulence structure around a circular, cylinder placed in an open channel ($D/H = 0.325$, H is the flow depth) with an approaching flow containing a steady current component superimposed on an unimodal oscillatory flow component. For these conditions (e.g., $H/D \approx 3$), one expects flow shallowness to have negligible effects on the dynamics of the shed wake vortices and horseshoe vortices. Detached eddy simulations (DES) are conducted with $0 \leqslant U_s' \leqslant 1.4$ such that the study investigates the two relevant regimes for a cylinder placed in combined wave-current flows. In the first regime, the approaching flow does not change direction while in the second regime the approaching flow changes direction during the oscillatory cycle.

The overall goal of the paper is to clarify the fundamental physics of flow past a surface-mounted cylinder in combined wave-current flow, which is the regime of relevance for most practical applications (e.g., scour phenomena at monopiles for offshore wind turbines) in coastal and maritime engineering. For this regime of great practical importance, there is much less information on the fundamental physics of the flow and erosion mechanisms compared to the canonical cases of a cylinder in steady flow or in purely oscillatory flow. As such, a main goal of the paper is to describe how the number of vortices shed during each half of the oscillatory cycle change with increasing U_s' and to describe the dynamics of these vortices for the same range of KC numbers considered in the companion study of [17]. The second goal is to understand how the dynamics of the horseshoe vortices changes between the limiting cases of purely oscillatory flow and of steady current. The third main goal is to describe how the relative importance of the main sediment entrainment mechanisms changes with the KC number and U_s'. The final goal is to describe how the variations of the phase-averaged streamwise (in-line) and spanwise drag forces acting on the cylinder change with increasing U_s' and to determine if Morrison's equation can still provide reasonable estimates of the oscillatory part of the in-line force for cases with a nonzero steady current component.

The numerical method, the boundary conditions and the main flow and geometrical parameters of the test cases are presented in Sec. II. Section III analyzes the changes in the number and dynamics of the shed wake vortices and the dynamics of the horseshoe vortices with varying KC number and U_s'. Section IV focuses on the effects of the KC number and U_s' on the bed shear stress distributions. The same section discusses the effects of the main types of coherent structures on the bed shear stresses. Section V investigates the effect of the same two parameters on the forces acting on the cylinder along the streamwise and spanwise directions. Section VI summarizes the main findings and presents some conclusions.

II. NUMERICAL MODEL, BOUNDARY CONDITIONS, AND TEST CASES

DES is a nonzonal hybrid RANS-LES method that can successfully predict complex turbulent flows and, in particular, separated flows (e.g., see [46]). DES has been extensively used to predict flow and turbulence structure past surface-mounted cylinders placed in steady current (e.g., see [10,12,16,44,47–50]). The accuracy of DES for this type of flows is similar to that of LES with a dynamic Smagorinsky model [10]. In particular, DES was shown to accurately capture the dynamics of the horseshoe vortices, including the bimodal oscillations of the main horseshoe vortex, and the wake dynamics for cases when the attached boundary layers were either laminar or turbulent at separation. Reference [17] showed that DES predicted more accurately compared to unsteady RANS the amplification of the bed shear stress beneath the horseshoe vortex forming around the base of a cylinder placed in oscillatory flow. Moreover, DES predictions of the wake dynamics for the oscillatory flow cases were consistent with experimental observations. Given that the present numerical model using DES was extensively validated for both surface-mounted cylinders in steady current and in purely oscillatory flow and that the level of mesh refinement in these previous simulations (e.g., [17]) is basically the same as the one used to conduct the present combined wave-current simulations, one can confidently use the same numerical solver to study the physics of cylinders placed in combined wave-current flow.

The delayed version of DES [51] is used to conduct the present simulations. This version of DES has the advantage that it preserves the RANS mode inside the attached boundary layers. The base model is the standard $k-\omega$ SST model [52]. The switch from RANS mode to LES mode is done by redefining the turbulence length scale in the expression for the dissipation rate in the transport equation for the turbulence kinetic energy, k, as $d_{\mathrm{DES}} = C_{\mathrm{DES}}\Delta$, where the grid size Δ is chosen as the minimum grid spacing along the three directions. The model constant is $C_{\mathrm{DES}} = 0.61$. The first grid point off the solid surfaces is placed inside the viscous sublayer, which avoids the use of wall functions.

To generate a combined unidirectional steady current-oscillatory flow, an unsteady forcing term, f_x, is added to the streamwise momentum equation. The filtered momentum equations are

$$\frac{\partial u_i}{\partial t} + \frac{\partial(u_i u_k)}{\partial x_k} = -\frac{\partial p}{\partial x_i} - \frac{\partial}{\partial x_k}\left[(\nu+\nu_t)\left(\frac{\partial u_i}{\partial x_k} + \frac{\partial u_k}{\partial x_i}\right)\right] + f_x\delta_{i1}, \tag{1}$$

where u_i is the instantaneous velocity component along the i direction, x_i is the i coordinate ($x_1 = x$, $x_2 = y$, $x_3 = z$), ν_t is the subgrid-scale viscosity, p is the instantaneous pressure, δ_{ij} is the Kronecker symbol, and $i = 1$ corresponds to the streamwise direction along which the forcing is applied. A finite-volume method is used to integrate the discretized incompressible Navier-Stokes equations and the modified $k-\omega$ SST model equations. The Gauss divergence theorem is used to convert volume integrals to surface integrals. A collocated grid layout is used. The convective terms in the momentum equations are discretized using a blend of the second-order accurate upwind biased

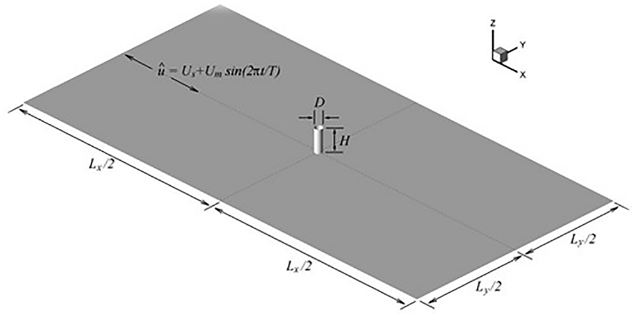

FIG. 1. Sketch of the computational domain with the main physical dimensions. The depth-averaged streamwise velocity at large distances from the cylinder is $\hat{u}$.

scheme and the second-order central scheme. A procedure similar to the classical algorithm of [53] is used to estimate the advecting velocity at each integrating point where a higher-order pressure redistribution term, that scales with the mesh spacing, is added. The second-order backward upwind scheme is used for time integration. A fully implicit discretization of the governing equations is used at each time step. Algebraic multigrid and the lower-upper factorization technique are used to solve the discrete system of linearized equations.

Figure 1 shows a sketch of the computational domain. The cylinder is placed at the center of the domain of length $L_x = 20H$ and width $L_y = 10H$. The origin of the system of coordinate is situated along the vertical axis of the cylinder at the bed level ($z = 0$). The top boundary is situated at $z = H(z' = z/H = 1)$. Periodic boundary conditions are applied in the streamwise direction. Consistent with previous numerical investigations of flow past surface-mounted cylinders (e.g., see [12,17]), slip-wall boundary conditions are imposed at the two lateral boundaries for the velocity components. No-slip boundary conditions are imposed at the bed and on the cylinder's surface. At the smooth walls, the boundary condition for the turbulent kinetic energy is $k = 0$. The turbulent viscosity at the smooth walls is calculated using the standard formula used with the $k - \omega$ model [54]. The top boundary is modelled as a shear-free slip wall (see also [5,17]). The gradients of the turbulence variables in the direction normal to the top and lateral boundaries are assumed to be zero. The nondimensional time step was $0.001TU_m/H$. After the initial transients were eliminated, phase-averaged quantities were collected over a time interval of at least 20 cycles. The computational domain was meshed using 5 million cells with 55 points in between the bed and the top boundary. The mesh was refined near the cylinder and close to the bed surface. Away from the cylinder and the bed, typical values of the Courant number when the magnitude of the approaching flow is the highest are close to 0.03.

Simulations were conducted with $1.5 \leqslant \mathrm{KC} \leqslant 30.8$ and $0 \leqslant U_s' \leqslant 1.4$ and with constant $D/H = 0.325$ and $\mathrm{Re}_m = DU_m/\nu \approx 130\,000$. The cylinder Reynolds number defined with the steady current velocity, $\mathrm{Re}_s = DU_s/\nu$, varied between 0 and 180 000. The Reynolds number defined with with the semi-excursion length, $a = U_mT/2\pi$, and the maximum velocity of the oscillatory component, $\mathrm{Re}_a = aU_m/\nu$, varied between 31 050 and 637 600 (Table I). The expression of the nondimensional forcing term in Eq. (1) was $f_x' = f_xT/U_m = a_x \cos(2\pi t/T) + b_x$. The two coefficients were calibrated for each case such that the nondimensional, depth-averaged streamwise velocity in the undisturbed flow was $\hat{u}' = \hat{u}/U_m = U_s' + \sin(2\pi t/T)$. For all cases, the nondimensional amplitude of the oscillatory forcing component was $a_x/(U_m\omega) = 1$, where $\omega = 2\pi/T$ is the angular frequency. Formally, one can consider that the simulations were performed with constant values of *D, H,* and U_m and varying periods of the oscillatory cycle, T and of the steady flow component, U_s. The undisturbed flow velocity $\hat{u}$ reaches its maximum value, $U_s + U_m$, and minimum value, $U_s - U_m$, at $t = T/4$ and $t = 3T/4$, respectively. For the simulations conducted with a nonzero steady current

TABLE I. Main nondimensional variables for the test cases.

$KC = TU_m/D$	U_s'	$U_s/(U_s + U_m)$	$Re_s = DU_s/\nu$	$Re_a = aU_m/\nu$	TU_m/H	$\tau_m/\rho U_m^2$
1.5	0.0	0	0	31 050	0.5	0.0043
1.5	0.4	0.286	5.2×10^4	31 050	0.5	0.0045
1.5	1.0	0.5	1.3×10^5	31 050	0.5	0.0066
1.5	1.4	0.583	1.8×10^5	31 050	0.5	0.0093
15.4	0.0	0	0	318 800	5	0.0027
15.4	0.4	0.286	5.2×10^4	318 800	5	0.0035
15.4	1.0	0.5	1.3×10^5	318 800	5	0.0056
15.4	1.4	0.583	1.8×10^5	318 800	5	0.0083
30.8	0.0	0	0	637 600	10	0.0024
30.8	0.4	0.286	5.2×10^4	637 600	10	0.0030
30.8	1.0	0.5	1.3×10^5	637 600	10	0.0057
30.8	1.4	0.583	1.8×10^5	637 600	10	0.0078

component, the upstream and downstream sides of the cylinder are defined with respect to the direction of the steady component. Over the first half of each cycle ($0 < t < T/2$), $\hat{u}' = \hat{u}/U_m > U_s'$, while over the second half ($T/2 < t < T$), $\hat{u}' < U_s'$. For the simulations conducted with a zero steady current component, the upstream (horseshoe vortex) side and the downstream (wake) side of the cylinder are defined with respect to the direction of the oscillatory flow. The maximum phase-averaged bed shear stress recorded during the oscillatory cycle in the undisturbed flow, τ_m, is also given in Table I.

About 4 weeks of simulation time on 64 processors of a PC cluster were needed for the flow to become quasiperiodic. Another 5–7 weeks were needed to calculate the phase-averaged flow over at least 20 oscillatory cycles. This corresponds to about 120 000 CPU hours per simulation.

III. EFFECTS OF THE KC NUMBER AND OF THE CURRENT VELOCITY TO OSCILLATORY VELOCITY RATIO ON LARGE-SCALE COHERENT STRUCTURES

A. Shed wake vortices

The vortical structures present in the instantaneous flow near the cylinder are visualized in Figs. 2 to 5 using a Q isosurface. The Q variable [$Q = -0.5\,(\frac{\partial u_i}{\partial x_j}\frac{\partial u_j}{\partial x_i})(H^2/U_m^2)$] is the second invariant of the velocity gradient tensor [55]. The phase-averaged and instantaneous vertical vorticity distributions in a horizontal ($z/H = 0.5$) plane in Figs. 6 and 7 provide additional information on the shed vortices and on their dynamics. Finally, Fig. 8 provides quantitative information on the lifespan of the shed vortices and the temporal variation of the coherence of these vortices as measured by the circulation inside their cores.

1. Low values of the KC number

Here, the low KC number regime is classified based on purely oscillatory flow cases where no vortices are shed in the wake during the oscillatory cycle. Of course, as the steady component increases, vortices will be shed on the downstream side of the cylinder, but their formation is due to the steady component.

In the case of purely oscillatory flow ($U_s' = 0$) with $KC = 1.5$, the wake flow is symmetric at all times with respect to the symmetry plane ($y/D = 0$). This is because for low KC numbers the approaching flow changes direction too fast for sufficiently coherent vortex tubes to form inside the separated shear layers on the downstream side of the cylinder. This is a prerequisite for wake vortices to form. Even in the $KC = 1.5$, $U_s' = 0.4$ case, where the steady current component is smaller than the maximum orbital velocity away from the cylinder ($U_s < U_m$), the wake flow

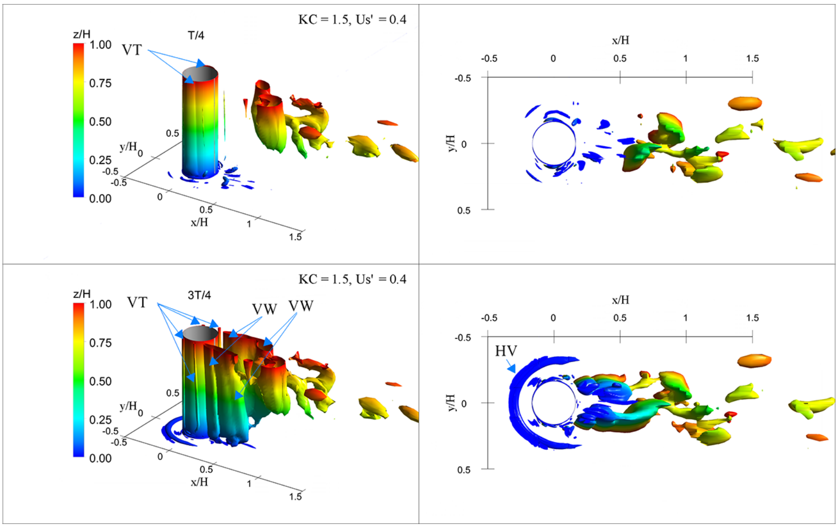

FIG. 2. Visualization of the coherent structures in the instantaneous flow fields in the KC = 1.5, $U_s' = 0.4$ simulation at $t = T/4$ (top), and $t = 3T/4$ (bottom). The Q isosurface ($Q = 5.0$) is colored with the distance from the channel bottom, $z' = z/H$. Besides the 3D view, a vertical view from below the channel bed is included to better visualize the near-bed (dark blue) vortices that are parallel to the channel bottom. To facilitate discussion of the effect of vortical structures on the bed shear stress distributions, the vertical views are rotated by 180° around the x axis. The horseshoe vortices, horizontal secondary vortices, vortex tubes, and main wake billow vortices are denoted HV, HSV, VT, and VW, respectively.

changes dramatically with respect to the $U_s' = 0$ case, as can be seen from Fig. 2 where several large-scale eddies are present. More specifically, several wake billow vortices (VWs) are present on the downstream side of the cylinder at $t = 3T/4$ ($\hat{u}' = -0.6$) while smaller symmetric pairs of vortex tubes (VTs) are present inside the attached boundary layers. The symmetric wake shedding mode dominates inside the separated shear layers. This is in stark contrast to the purely oscillatory flow case with KC = 1.5 where no such coherent structures are generated in the instantaneous flow fields. This is also why no results were included in Fig. 2 for this case.

Analysis of the instantaneous flow fields and phase-averaged vertical vorticity, $\overline{\omega_z}$, in the KC = 1.5 $U_s' = 0.4$ case, shows that two pairs of symmetric vortex tubes form on the downstream side of the cylinder during the first half of each oscillatory cycle [e.g., see $\overline{\omega_z}$ distribution at $t = 7T/8$ in Fig. 6(a)]. The temporal evolution of the phase-averaged nondimensional circulation of these two pairs of vortices forming on the downstream side of the cylinder, DV1 and DV2, is shown in Fig. 8(a). The circulation is estimated based on the distribution of the vertical vorticity at the free surface. These vortices form around $t = 0.375T$ and 0.5T, respectively, after the approaching flow reaches its peak (positive) value at $t = 0.25T$. After their formation, the coherence of DV1 and DV2 is comparable [Fig. 8(a)]. Once the approaching flow reverses, DV1 and DV2 remain on the same side of the cylinder where they originated. Because of the change in the direction of the approaching flow, the two co-rotating vortices merge around $t = 0.875T$, which explains the increase in the circulation of the merged vortex at $t = 0.875T$. The merged vortex diffuses around $t = 1.125T$ such that for a short time during the oscillatory cycle ($t \approx 0.125T$–$0.25T$) no VW vortices are present. Similar to the purely oscillatory flow cases, the cores of the shed wake vortices (e.g., DV1 and DV2), remain close to vertical during their lifetime (e.g., see flow field at $t = 3T/4$ in Fig. 2). During the time the incoming flow is negative, a symmetric pair of vortex tubes (VT) forms on the upstream side of the cylinder starting at $t = 3T/4$ when $\hat{u}$' reaches its peak negative value. This pair is also visualized in Fig. 6(a) at $t = 7T/8$. Then the UV1 pair starts moving toward

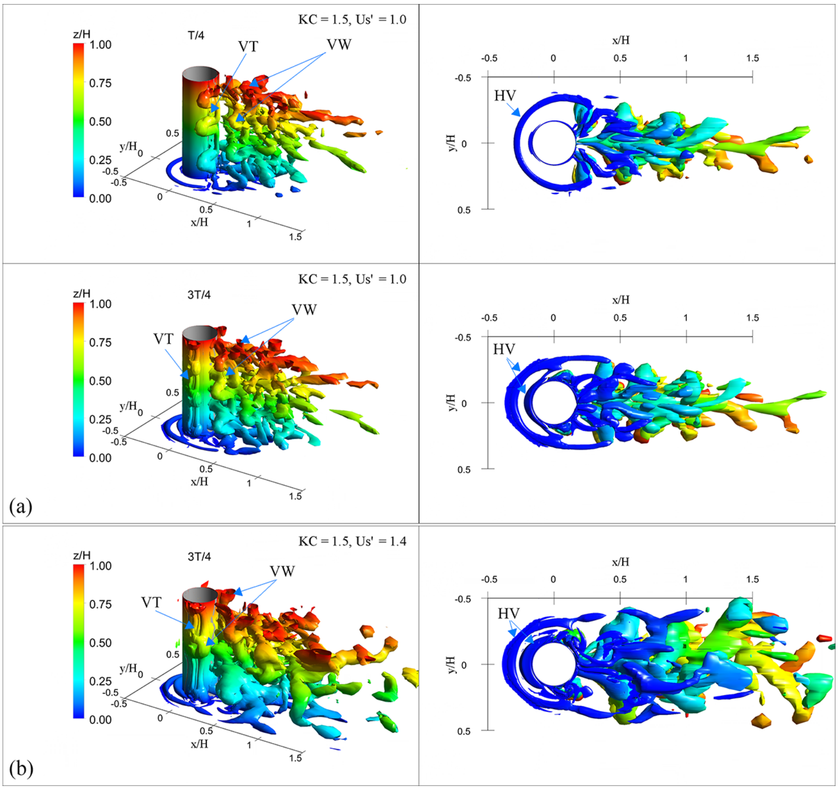

FIG. 3. Visualization of the coherent structures in the instantaneous flow fields. (a) KC $= 1.5$, $U_s' = 1.0$; (b) KC $= 1.5$, $U_s' = 1.4$. See also caption of Fig. 2.

the other side of the cylinder once the incoming flow reverses [e.g., see frame at $t = T/8$ in Fig. 6(a) corresponding to $t = 1.125T$ in Fig. 8(a)], but the vortex tubes never detach from the cylinder and disappear around $t = 1.25T$ [Fig. 8(a)].

In the KC $= 1.5$, $U_s' = 1.0$ case, the approaching flow is at all times oriented toward the upstream side of the cylinder with $\hat{u}' = 0$ at $t = 3T/4$. This explains why no shedding takes place on the upstream side. On the downstream side, a pair of countervortices vortices is shed each cycle [DV1 in Fig. 6(b)]. The vortices form around $t = T/2$ [Fig. 8(b)], with the symmetric shedding mode being dominant. After their formation these vortices remain in the vicinity of the cylinder and their circulation increases due to merging with vortex tubes generated in the attached boundary layer. The pair of vortices detaches from the cylinder at the start of the next cycle when and their circulation peaks at $t = 1.25T$ [Fig. 8(b)]. Then, their circulation monotonically decreases as their cores move slowly away from the cylinder. This is also why vortices generated in previous cycles are still visible inside the near wake [Fig. 6(b)]. So the increase of U_s' from 0.4 to 1.0 did not result in an increase of the number of shed vortices on the downstream side of the cylinder.

As expected, no vortices are shed on the upstream side of the cylinder in the KC $= 1.5$, $U_s' = 1.4$ case. Similar to the KC $= 1.5$, $U_s' = 1.0$ case, only one pair of symmetric vortices is shed on the downstream side during each oscillatory cycle. These vortices detach from the cylinder around $t = 3T/4$ [Figs. 3(b) and 6(c)] when the magnitude of the approaching flow is the smallest ($\hat{u}' = 0.4$). The main effect related to increasing U_s' from 1.0 to 1.4 is the increase of the circulation of the shed vortices (e.g., the increase is close to 80% for the peak circulation). Despite the large deformations of their cores, the shed vortices from the previous cycles maintain their coherence as they are advected away from the cylinder, which explains the presence of several billow vortices

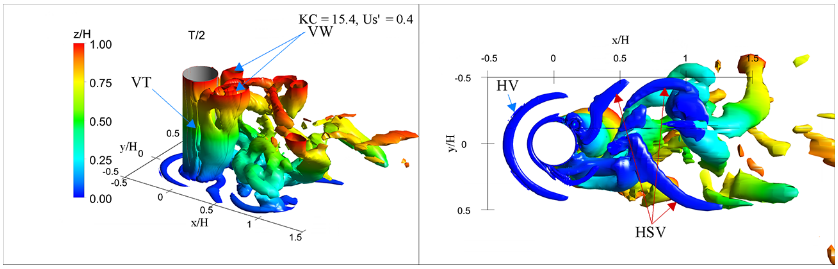

FIG. 4. Visualization of the coherent structures in the instantaneous flow fields in the KC = 15.4, $U_s' = 0.4$ simulation. See also caption of Fig. 2.

inside the downstream wake in Fig. 6(c). The original symmetry of the pair of shed vortices is lost as these vortices are advected downstream and interact with surrounding eddies.

The instantaneous flow fields in the KC = 1.5 simulations with $U_s' = 1.0$ and $U_s' = 1.4$ also show the formation of large-scale hairpin-like eddies along the cores of the vortex tubes as they are still in contact with the cylinder (Fig. 3). This explains the strong deformations of the cores of the shed vortices in this case, a phenomenon that is not present in any of the simulations conducted with purely oscillatory flow. The mechanism for the formation of these hairpin-like eddies bears some similarities with the Corcos-Lin instability where hairpin-like vortices are generated along the core of a less coherent (e.g., lower circulation), smaller-size vortex situated in between two larger, more coherent, vortices as the three vortices are advected by the flow. In the present case, it is the deformed core of the larger shed vortex that induces the formation of the hairpins along the core of the smaller vortex tube while the vortex tube is still attached to the cylinder. As a result of the growth of this instability, the cores of the main coherent structures inside the near wake are subject to large deformations along the vertical direction. This instability is the strongest for $U_s' \approx 1.0$ [Fig. 3(a)]. Such hairpins are also present in the KC = 1.5, $U_s' = 1.4$ case [Fig. 3(b)]. However, the hairpins are smaller compared to the ones forming in the KC = 1.5, $U_s' = 1.0$ case where the distance between their head and the separation line before they detach from the cylinder is close to D/2. The vertical spacing (e.g., wavelength) of the hairpins is close to 1.0D for $U_s' = 1.0$ and 1.4D for $U_s' = 1.4$. As the steady flow component starts dominating, this instability weakens due to the increase of the wavelength and decrease of the amplitude of the deformations of the vortex tube before separation occurs.

2. *High values of the KC number*

In the case of purely oscillatory flow, the antisymmetric wake shedding mode dominates for KC > 10. Reference [17] found that, over most cycles, one billow vortex is shed from each side of the cylinder during each oscillatory cycle for KC = 15.4 and three billow vortices are always shed from each side of the cylinder for KC = 30.8. This result is consistent with other studies that have shown that the number of shed vortices increases with the KC number [19,26]. For KC = 15.4, the vortex shed on one side was then advected over the other side during the next half of the oscillatory cycle. In all the present KC = 15.4 and KC = 30.8 simulations with a steady current, the shedding of wake vortices is antisymmetric on both sides of the cylinder.

In the KC = 15.4, $U_s' = 0.4$ case, four billow vortices (DV1 to DV4) are shed between $t = 0.125T$ and $t = 0.5T$ on the downstream side. The peak circulation of these vortices is comparable [Fig. 8(c)]. The first two vortices shed during the first half of the oscillatory cycle (DV1 and DV2) are visible in Fig. 4 and in the phase-averaged vorticity field at $t = T/4$ in Fig. 7(a) where the pair of vortices appears to be symmetric. This is because of the phase averaging as if a vortex forms on the right side in one cycle it will then form on the left side in the next cycle. Rather than moving downstream, the last vortex shed during the first half of the oscillatory cycle is advected over the upstream side of the cylinder once the incoming flow changes direction and loses its coherence around $t = 0.75T$ [see DV4 in Fig. 8(c)]. Another interesting observation and difference with respect to the corresponding low KC number case [Fig. 8(a)] is that the shed wake billow vortices lose their coherence much faster [e.g., by $t = 0.75T$, Fig. 8(c)] once the incoming flow starts decelerating and reverses its orientation. Also present in Fig. 7(a) at $t = 3T/4$ is a pair of small antisymmetric vortices, UV1, forming on the upstream side of the cylinder. This vortex detaches from the cylinder and initially moves away from it. As the approaching flow changes sign, the UV1 vortex starts moving on the opposite direction, close to the lateral side of the cylinder, and from there UV1 is advected on the downstream side where it disappears around $t = 1.125T$ [Fig. 8(c)].

For $U_s' = 0.4$, the main effect of increasing the KC number value from 15.4 to 30.8 is to increase the number of shed vortices on the two sides of the cylinder [e.g., from four to six on the downstream side and from one to two on the upstream side; see Figs. 8(c) and 8(e)]. The peak circulation of the vortices shed on the downstream side is comparable in the two simulations. However, the vortices shed near the time when the approaching flow velocity peaks (e.g., DV2 and DV3) are of lower coherence in the KC = 30.8 simulation. The first four vortices are shed during the time the incoming flow accelerates [e.g., see DV1 to DV4 at $t = T/4$ in Figs. 7(b) and 5(a)], while the last two vortices are shed during the time the approaching flow decelerates ($T/4 < t < T/2$). The shedding frequency peaks around $t = T/4$. Also, none of these vortices moves on the other side of the cylinder during the next half cycle. Similar to the corresponding KC = 15.4 case, the DV vortices lose their coherence fairly rapidly as the approaching flow decelerates and changes direction. This is also an important difference with respect to the wake dynamics observed in the KC = 1.5 cases. On the upstream side, the first shed vortex, UV1, remains on side where it originated [see $\overline{\omega_z}$ at $t = 3T/4$ in Fig. 7(b)], while the second one, UV2, is advected on the downstream side after the approaching flow reverses.

No vortices are shed on the upstream side in the $U_s' = 1.0$ simulations [Figs. 8(d) and 8(f)]. For both KC numbers, the number of anti-symmetrical vortices shed on the downstream side increases with U_s'. The same is true for the coherence and the lifespan of most of these vortices. For example, in the simulations conducted with KC = 15.4, the number of shed vortices on the downstream side increases from four to seven [Figs. 8(c) and 8(d)], while the peak circulation of some of the DV vortices in the $U_s' = 1.0$ simulation is more than twice that of the vortices forming in the $U_s' = 0.4$ simulation. The number of DV vortices in the KC = 30.8 simulations increases from six ($U_s' = 0.4$) to eight ($U_s' = 1.0$), while the peak circulation of some of these vortices is close to four times larger in the $U_s' = 1.0$ simulation compared to the corresponding $U_s' = 0.4$ simulation.

For $U_s' = 1.0$, the changes in the wake structure on the downstream side due to the increase of the KC number from 15.4 [Fig. 8(d)] to 30.8 [Fig. 8(f)] are qualitatively similar to those observed in the corresponding $U_s' = 0.4$ simulations [e.g., increase in the number and coherence of the DV vortices; see also Figs. 7(b) and 7(d) that visualize some of the DV vortices at $t = T/4$]. Most of the DV vortices are shed over the first half of the oscillatory cycle in the high KC number, $U_s' = 1.0$ simulations. The shedding frequency of the DV vortices is fairly constant in the KC = 30.8, $U_s' =$ 1.0 simulation despite the fact that the coherence of these vortices when they are shed is highly variable. Interestingly, the highest circulation DV vortices are those shed after the incoming flow velocity reaches its maximum value, $\hat{u}$' = 2.0 at $t/T = 0.25$ [Figs. 8(d) and 8(f)].

The differences in the wake dynamics are even smaller when the high KC number simulations with $U_s' = 1.0$ [Fig. 5(b)] and $U_s' = 1.4$ [Fig. 5(c)] are compared. For KC = 30.8, the number of shed vortices remains the same but the peak circulation of some of the DV vortices increases with up to 50% in the KC = 30.8, $U_s' = 1.4$ case [Fig. 8(g)] compared to the KC = 30.8, $U_s' = 1.0$ case [Fig. 8(f)]. The same is true for the lifetime of some of the DV vortices. Similar trends were observed in the corresponding KC = 15.4 simulations.

B. Horseshoe vortices and other near-bed vortices

Near-bed coherent structures that include horseshoe vortices (HVs) on the upstream side and nearly-horizontal vortices on the wake side are generated in the combined wave-current cases.

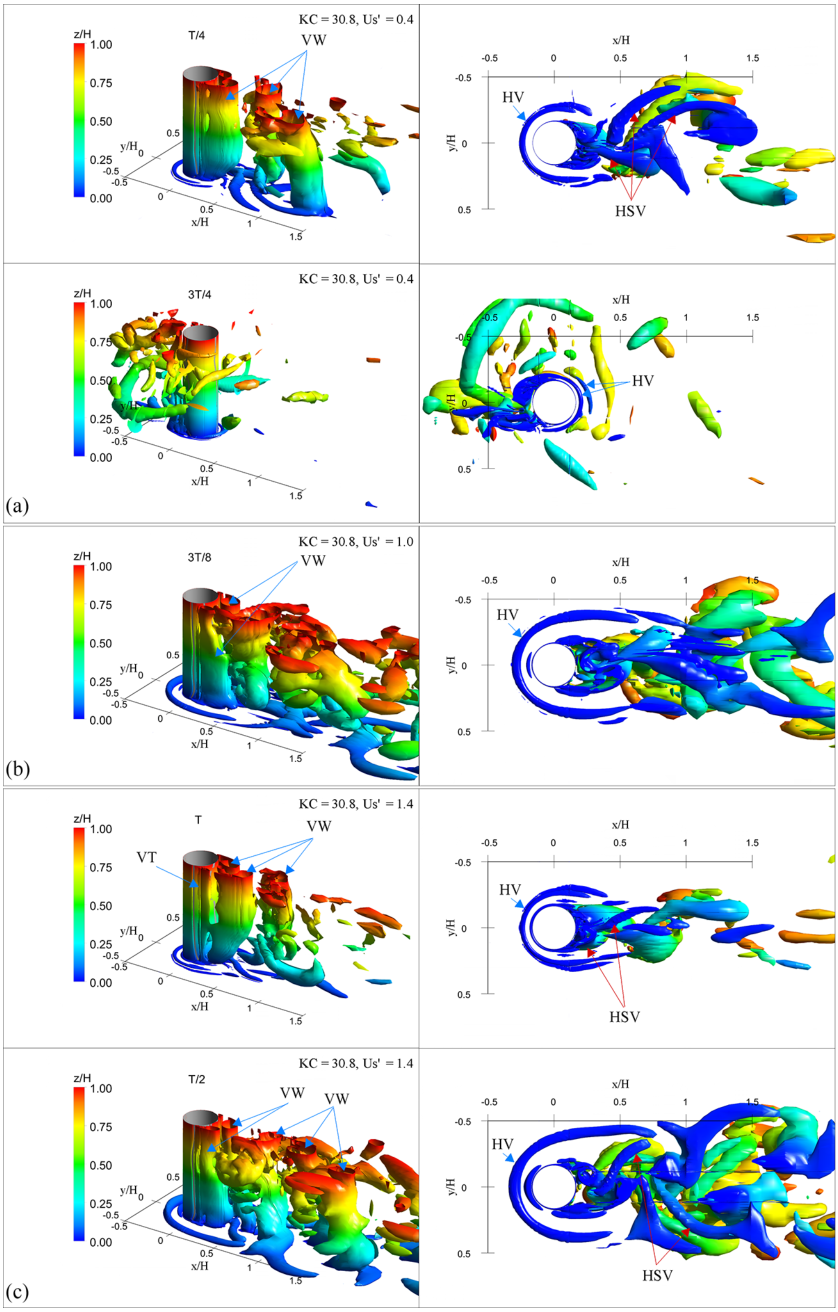

FIG. 5. Visualization of the coherent structures in the instantaneous flow fields. (a) KC = 30.8, $U_s' = 0.4$; (b) KC = 30.8, $U_s' = 1.0$; (c) KC = 30.8, $U_s' = 1.4$. See also caption of Fig. 2.

1. Low values of the KC number

No HVs form in the purely oscillatory case with KC = 1.5 [17]. Present simulations show that the presence of a weak steady current component results in the formation of horseshoe vortices. For example, a well-defined HV, whose core it is situated outside of the bottom boundary layer,

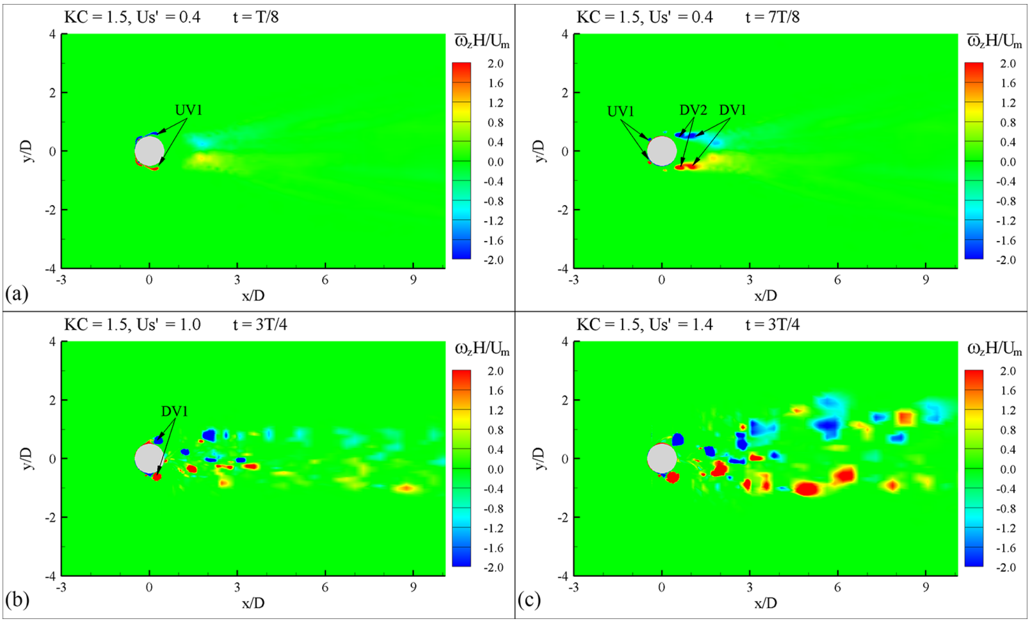

FIG. 6. Nondimensional phase-averaged and instantaneous vertical vorticity in the $z/H = 0.5$ plane. (a) $\overline{\omega_z} H/U_m$ at $t = T/8$ ($\hat{u}' = 1.1$) and $t = 7T/8$ ($\hat{u}' = -0.32$) for KC = 1.5, $U_s' = 0.4$; (b) $\omega_z H/U_m$ at $t = 3T/4$ ($\hat{u}' = 0$) for KC = 1.5, $U_s' = 1.0$; (c) $\omega_z H/U_m$ for $t = 3T/4$ ($\hat{u}' = 0.4$) for KC = 1.5, $U_s' = 1.4$.

is present for $0.3T < t < 0.5T$ in the KC = 1.5, $U_s' = 0.4$ case. One should note that the Q criterion indicates the presence of a horseshoe-like vortical structure over a larger part of the cycle. However, this structure is not really a well-defined vortex with a core of high vorticity separated from the bottom boundary layer and with streamlines converging toward its core. The methodology to identify the presence of a HV is consistent with the one used by [19] based on analysing the phase-averaged flow fields in the symmetry plane ($y/D = 0$) of the cylinder. The HV vortex is not present in the flow field at $t = T/4$ when $\hat{u}$' reaches its maximum value (Fig. 2). Its lifetime is about $0.2T$, which is the value reported by [19] for slightly larger values of the KC number for $U_s' = 0.3{-}0.41$. No HVs are generated on the downstream side.

The lifetime of the main HV on the upstream side of the cylinder increases to about $0.4T$ and $0.65T$ in the simulations performed with $U_s' = 1.0$ and $U_s' = 1.4$, respectively. The value in the KC = 1.5, $U_s' = 1.0$ simulation ($0.4T$) is close to the one ($0.375T$) reported by [19] at a slightly higher KC number and for $U_s' = 0.82$. No combined wave-current flow experiments were conducted with $U_s' > 0.82$ by [19]. A weak secondary HV that remains in contact with the cylinder is present in the $U_s' = 1.0$ simulation [see flow field at $t = 3T/4$ in Fig. 3(a)]. A stronger secondary HV is generated from $t = 5T/8$ to $t = 7T/8$ next to the junction line in the $U_s' = 1.4$ simulation [see flow field at $t = 3T/4$ in Fig. 3(b)].

2. High values of the KC number

A main HV is generated over each half cycle in the $U_s' = 0$ simulations with KC = 15.4 and KC = 30.8. The lifetime and the circulation of the main HV increase with increasing KC number. Over the first half of each cycle, the HV is present from $T/8$ to $7T/16$ in the KC = 15.4 simulation and from $T/16$ to $7T/16$ in the KC = 30.8 simulation. The predicted lifetime of the main HV vortex in the KC = 15.4, $U_s' = 0.0$ simulation (0.375T) is within 10% of the value inferred from the oscillatory flow experiments of [19]. No comparison can be made for KC = 30.8 given that the KC number in the purely oscillatory and combined wave-current experiments of [19] was less than

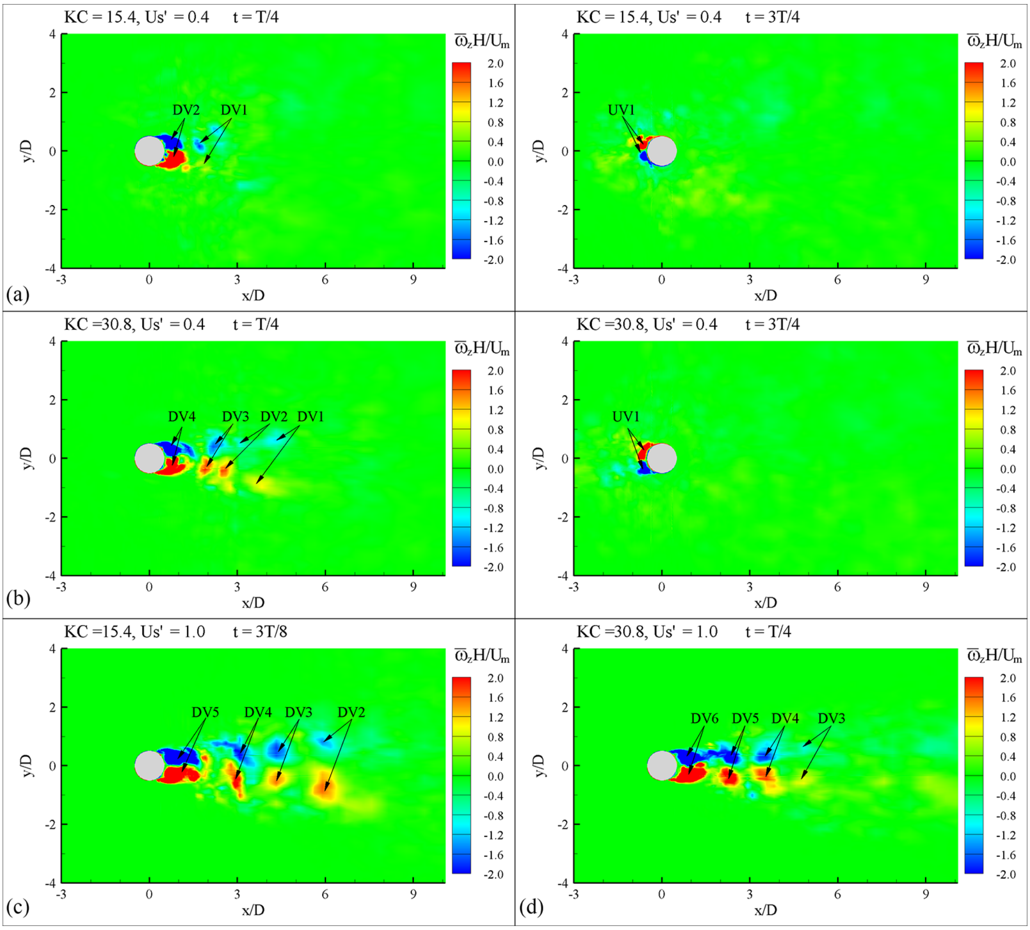

FIG. 7. Nondimensional phase-averaged vertical vorticity in the $z/H = 0.5$ plane. (a) $\overline{\omega_z}H/U_m$ at $t = T/4$ ($\hat{u}' = 1.4$) and $t = 3T/4$ ($\hat{u}' = -0.6$) for KC = 15.4, $U_s' = 0.4$; (b) $\overline{\omega_z}H/U_m$ at $t = T/4$ ($\hat{u}' = 1.4$) and 3T/4 ($\hat{u}' = -0.6$) for KC = 30.8, $U_s' = 0.4$; (c) $\overline{\omega_z}H/U_m$ at $t = T/4$ ($\hat{u}' = 2.0$) for KC = 15.4, $U_s' = 1.0$; (d) $\overline{\omega_z}H/U_m$ at $t = T/4$ ($\hat{u}' = 2.0$) for KC = 30.8, $U_s' = 1$.

20. The circulation of the HV starts decaying and its core moves away from the bed as the flow decelerates (e.g., see Fig. 10).

As opposed to the low KC number simulations with $U_s' \ll 1$, HVs may form on both sides of the cylinder in the high KC number simulations with $U_s' \ll 1$. This is the case of the KC = 30.8, $U_s' = 0.4$ simulation where a very weak HV is present for $0.75T \leqslant t \leqslant 0.875T$ [e.g., see flow field at $t = 3T/4$ in Fig. 5(a)]. However, no such vortex forms in the corresponding KC = 15.4 simulation. Only one HV forms on the upstream side of the cylinder in the KC = 15.4 and KC = 30.8 simulations [Figs. 4 and 5(a)]. Its lifespan increases with the KC number, from about 0.45T in the KC = 15.4 simulation to $0.55T$ in the KC = 30.8 simulation. For KC ≈ 15 and $U_s' = 0.3\text{–}0.41$, [19] reported a value of 0.48T. As opposed to the low KC number cases, the circulation of the main HV peaks during the time interval the incoming flow accelerates to reach its maximum value (Fig. 9). Similar to the corresponding cases with purely oscillatory flow, large, horizontal, near-bed vortices form in the high KC number simulations with $U_s' = 0.4$, but these vortices are present only on the downstream side of the cylinder [Figs. 4 and 5(a)].

The lifespan of the main HV continues to increase with increasing magnitude of the steady flow component. In the KC = 15.4 simulations, the lifespan increases from 0.45T for $U_s' = 0.4$

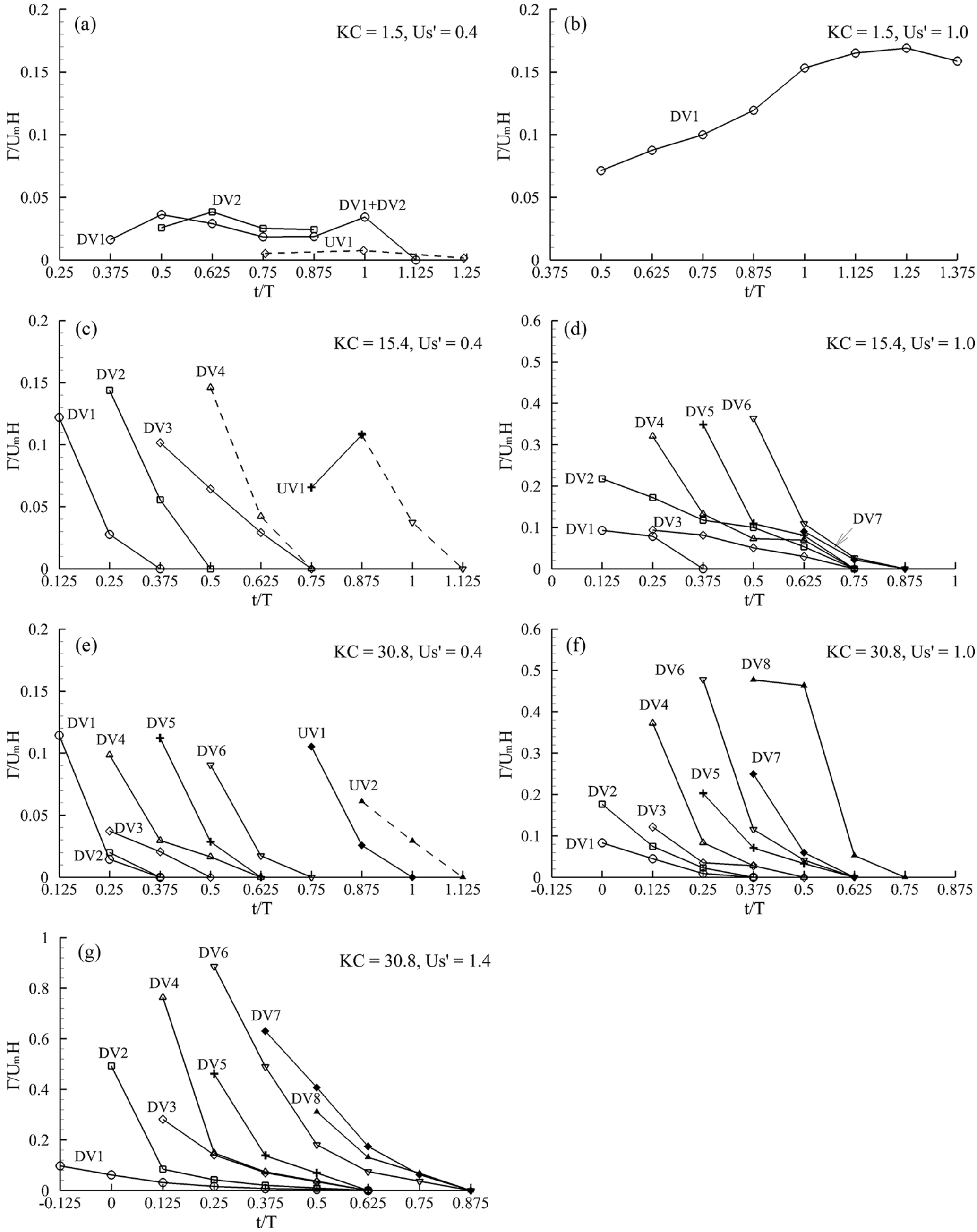

FIG. 8. Nondimensional phase-averaged circulation of wake vortices, Γ/U_mH, vs nondimensional time, t/T. (a) KC = 1.5 and $U_s' = 0.4$; (b) KC = 1.5 and $U_s' = 1.0$; (c) KC = 15.4 and $U_s' = 0.4$; (d) KC = 15.4 and $U_s' = 1.0$; (e) KC = 30.8 and $U_s' = 0.4$; (f) KC = 30.8 and $U_s' = 1.0$; (g) KC = 30.8 and $U_s' = 1.4$. A dashed line is used for vortices that are shed on one side but are then advected on the opposite side of the cylinder.

to 0.625T ($T/16 \leqslant t \leqslant 11T/16$) for $U_s' = 1.0$ and to 0.875T ($-T/8 \leqslant t \leqslant 3T/4$) for $U_s' = 1.4$. For KC $\approx$ 15, the data of [19] suggest the lifespan of the main HV vortex is slightly larger than 0.5T. In the KC = 30.8 simulations [Figs. 5(b) and 5(c)], the lifespan of the main HV is 0.68 T

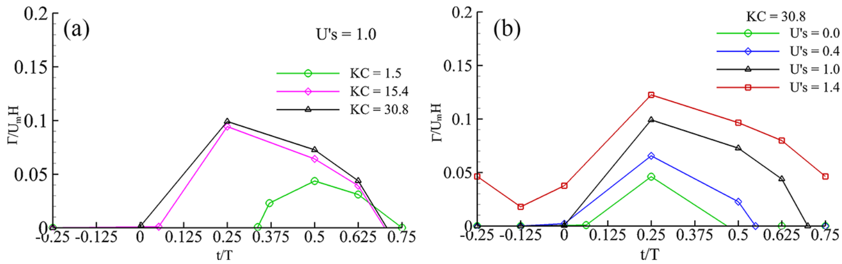

FIG. 9. Nondimensional phase-averaged circulation of main horseshoe vortex, Γ/U_mH, vs nondimensional time, t/T. (a) effect of varying the KC number in the simulations conducted with $U_s' = 1$; (b) effect of varying U_s' in the simulations conducted with KC = 30.8.

($0 \leqslant t \leqslant 11T/16$) for $U_s' = 1.0$ and about 1.0T for $U_s' = 1.4$, where the HV is present in all flow fields [see also Fig. 9(b)]. For same value of U_s', the lifespan of the main HV increases monotonically with KC [see also Fig. 9(a)]. While no secondary HV is present in the KC = 15.4 simulations, one weak secondary HV is present only in the KC = 30.8, $U_s' = 1.4$ simulation between $t = T/4$ and $t = 5T/8$ [e.g., see flow field at $t = T/2$ in Fig. 5(c)].

Figure 10 provides more details on the general dynamics of the main HV in a high KC number and high U_s' simulation based on the KC = 30.8, $U_s' = 1$ simulation results. The main HV vortex is generated very close to the cylinder, shortly after $t = 0T$. The size of the vortex and its circulation in the symmetry plane increase monotonically for $0 < t < T/4$. The circulation reaches its maximum value at $t = T/4$ [Fig. 10(a)]. While the circulation starts decreasing [Fig. 9(b)], the size of the core continues to increase as the approaching flow starts decelerating [Figs. 10(b) and 10(c)]. As this happens, the vortex moves away from the cylinder and the bed especially for $t > T/2$ when $\hat{u}$'

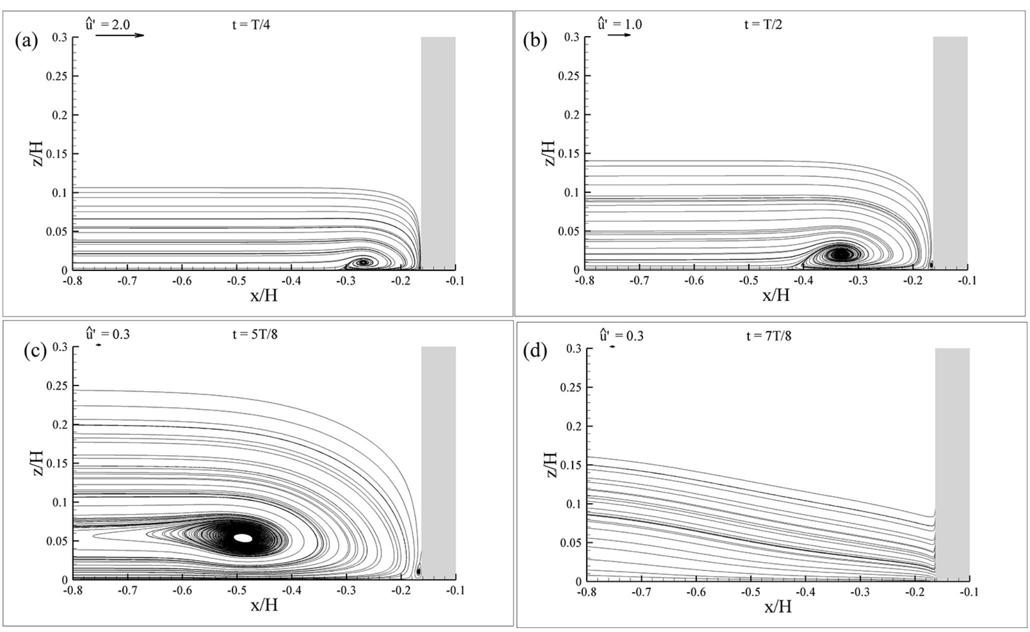

FIG. 10. Two-dimensional mean flow streamlines in the symmetry ($y/H = 0$) plane in the KC = 30.8, $U_s' = 1$ simulation showing the main horseshoe vortex in the phase-averaged flow. (a) $t = T/4$ ($\hat{u}' = 2$); (b) $t = T/2$ ($\hat{u}' = 1$); (c) $t = 5T/8$ ($\hat{u}' = 0.3$); (d) $t = 7T/8$ ($\hat{u}' = 0.3$).

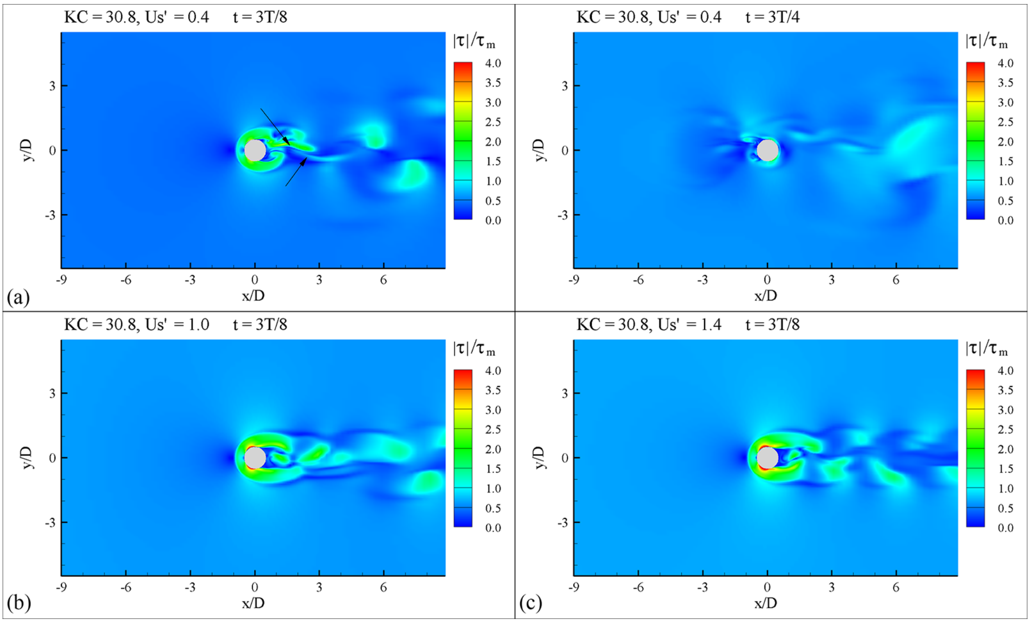

FIG. 11. Nondimensional bed shear stress magnitude $|\tau|/\tau_m$ in the KC $= 30.8$ simulations. (a) $t = 3T/8$ and $t = 3T/4$ for $U_s' = 0.4$; (b) $t = 3T/8$ for $U_s' = 1.0$; (c) $t = 3T/8$ for $U_s' = 1.4$. The black arrows in frame a point toward regions of high $|\tau|/\tau_m$ induced by horizontal near-bed vortices [see also Fig. 5(a)].

$< U_s'$ [e.g., see Fig. 10(c)]. This is followed by a rapid loss of its coherence around $t = 11T/16$. The vortex is not present from $t = 11T/16$ until close to $t = T$ [e.g., see Fig. 10(d)].

For constant U_s', the lifespan and peak nondimensional circulation of the main HV increase monotonically with increasing KC number at least until KC ≈ 15. This effect is illustrated in Fig. 9(a) for $U_s' = 1$ where the peak circulation increases by about 100% as the KC number varies from 1.5 to 15.4. For larger values of the KC number, the rate of increase of the HV circulation with increasing KC number is very low. Meanwhile, for constant KC number, the lifespan and peak circulation of the main HV increase monotonically with increasing U_s', as illustrated in Fig. 9(b) for KC $= 30.8$. The peak circulation increases by about 120% between the purely oscillatory cases and the simulation conducted with $U_s' = 1$. A further increase of U_s' to 1.4 results in an increase of about 20% of the peak circulation of the main HV. For KC $= 30.8$, the main HV is present over the whole oscillatory cycle starting with a minimum value of U_s' between 1.0 and 1.2. For all high KC number simulations, the peak circulation is recorded at $t = T/4$ (Fig. 9). By contrast, the peak circulation in the KC $= 1.5$ simulations where a HV is present occurs close to $t = T/2$ [Fig. 9(a)].

Though near-bed horizontal vortices are observed in all the high KC number simulations, the size of these vortices based on the Q criterion decreases slightly in the $U_s' = 1.4$ simulations compared to the $U_s' = 1$ simulations.

IV. BED SHEAR STRESSES

To allow a more meaningful comparison of the erosive potential of the flow between different cases, the distributions of the bed shear stress magnitude in Figs. 11 to 14 are normalized by τ_m which increases with U_s' (Table I). The main focus is on the high KC number simulations where the coherence and lifespan of the main HV are relatively high.

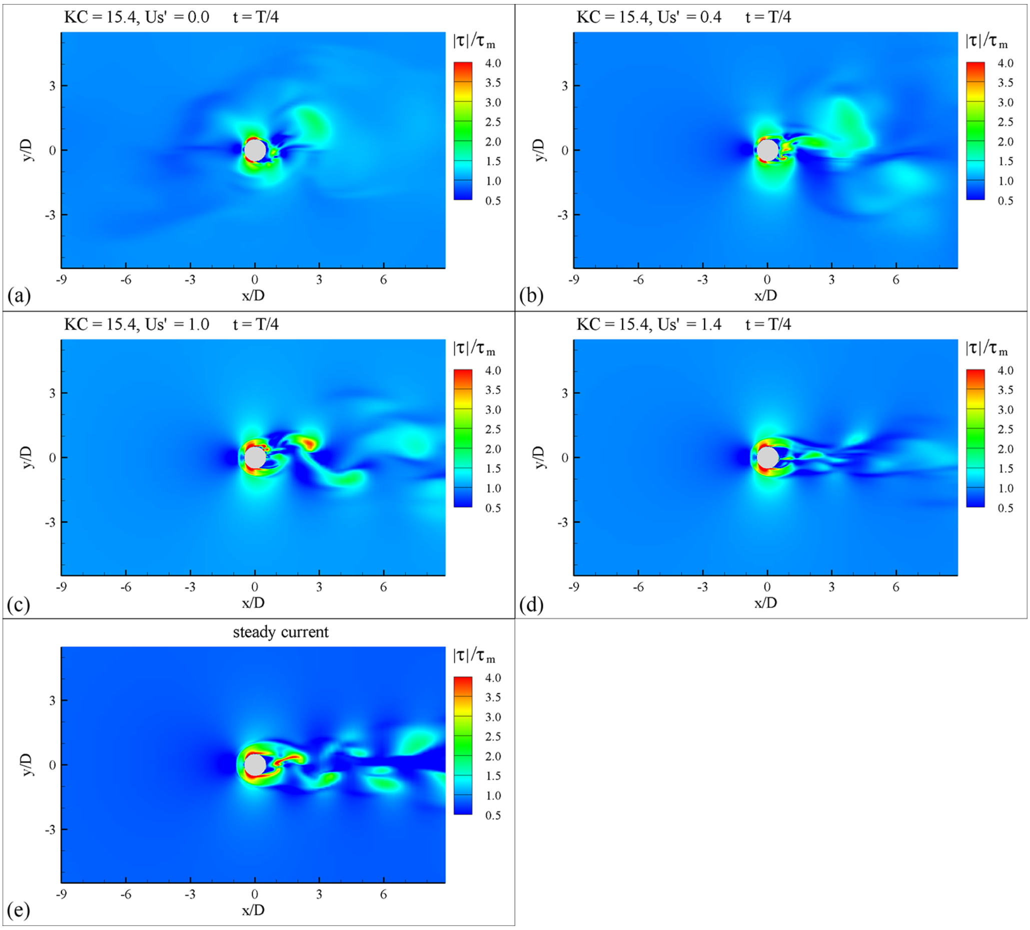

FIG. 12. Nondimensional bed shear stresses magnitude $|\tau|/\tau_m$ at $t = T/4$ in the KC = 15.4 simulations. (a) $U_s' = 0.0$; (b) $U_s' = 0.4$; (c) $U_s' = 1.0$; (d) $U_s' = 1.4$. Also shown in panel (e) are results from a steady current simulation with $U_s = U_m$.

A. Bed shear stress distributions during the oscillatory cycle

In the high KC number with $U_s' = 0.4$, the bed shear stress is strongly amplified during most of the first half of the oscillatory cycle in several regions [e.g., see distribution at $t = 3T/8$ in Fig. 11(a) for KC = 30.8 and at $t = T/4$ in Fig. 12(b) for KC = 15.4]. In both cases, a large increase of $|\tau|/\tau_m$ is observed beneath the cores of the main wake billow vortices, the separated shear layers and the horizontal near-bed vortices on the downstream side of the cylinder and beneath the main HV on the upstream side. This can be best observed in Fig. 11(a) that shows $|\tau|/\tau_m$ at $t = 3T/8$ for the KC = 30.8, $U_s' = 0.4$ case [see also Fig. 5(a)]. Moreover, the bed shear stress is amplified beneath the separated shear layers and the HV on the upstream side [see flow field at $t = 3T/4$ in Fig. 5(a) and $|\tau|/\tau_m$ in Fig. 11(a)] during part of the second half of the oscillatory cycle when the incoming flow reverses. Compared to the limiting case of a purely oscillatory flow, the size of the region of high bed shear stress values (e.g., $|\tau|/\tau_m > 1.3$) increases on the wake side and on the lateral sides of the cylinder at $t = T/4$ when the erosive potential of the flow is the largest in the high KC number simulations [e.g., compare bed shear stress distributions in Figs. 12(a) and 12(b) for KC = 15.4].

As the steady current component in the high KC number simulations is increased from $0.4U_m$ to U_m, an overall increase of the magnitude of the bed shear stresses is observed inside the wake on the downstream side of the cylinder [e.g., compare Figs. 11(a), and11(b) at $t = 3T/8$ for the KC = 30.8 simulations and Figs. 12(b) and 12(c) for the KC = 15.4 simulations]. This increase is mainly driven by the increase in the number of billow vortices advected in the wake (e.g., compare $|\tau|/\tau_m$ at $t = 3T/8$ for the KC = 30.8, $U_s' = 1$ case in Fig. 11(b) and for the KC = 30.8, $U_s' = 0.4$ case in Fig. 11(a)). High values of $|\tau|/\tau_m$ are also induced in the KC = 15.4 and KC = 30.8 simulations with $U_s' = 1$ beneath the main HV at times when its coherence is relatively large, beneath the separated shear layers and beneath the horizontal, near-bed vortices forming on the downstream side of the cylinder.

The increase of U_s' from 1.0 to 1.4 in the KC = 30.8 simulations has a fairly negligible effect on the level of amplification of $|\tau|/\tau_m$ around the upstream face of the cylinder and inside the downstream wake [e.g., compare results at $t = 3T/8$ in Figs. 11(b) and 11(c)]. This is in part because the circulation of the shed vortices and the number of shed vortices during each oscillatory cycle remains about the same in the KC = 30.8 simulations with $U_s' = 1$ [Fig. 8(f)] and $U_s' = 1.4$ [Fig. 8(g)]. On the other hand, the average levels of $|\tau|/\tau_m$ inside the downstream wake decay in the KC = 15.4, $U_s' = 1.4$ case [Fig. 12(d)] compared to the KC = 15.4, $U_s' = 1$ case [Fig. 12(c)] over most of the oscillatory cycle. The main reason is the reduction of the number of shed vortices per oscillatory cycle from seven for $U_s' = 1.0$ to six for $U_s' = 1.4$ and a decrease of the circulation of most of the shed vortices.

For mixed wave-current flow, the bed shear stress distributions are qualitatively very different from those observed for steady current flow [Fig. 12(e)] especially at times when the velocity magnitude in the approaching flow is significantly lower than the peak approaching flow velocity. This is especially true for cases with $U_s' < 1$. Over the part of the cycle when the magnitude of the incoming flow is small, most of the entrainment is expected to occur beneath the HVs and the cores of the most coherent wake vortices with very little sediment entrained on the sides of the cylinder, as is the case for steady flow past a cylinder placed on a horizontal surface. If one compares results from high KC number simulations at times where the magnitude of the approaching flow peaks or is close to the peak [Figs. 12(c) and 11(b)] and steady current simulations conducted with same value of the steady component [Fig. 12(e)], the size of the region of high bed shear stress on the wake side is larger in the mixed wave-current flow simulations, while the levels of bed shear stress amplification beneath the main HV vortex and close to the sides of the cylinder are larger in the steady current simulation.

Large qualitative differences are observed between the high [e.g., see Figs. 13(b) and 13(d)] and the corresponding low KC number simulations [e.g., see Figs. 13(a) and 13(c)]. This is fully expected for the purely oscillatory case (KC = 1.5, $U_s' = 0$) where no HV vortex forms and no billow vortices are shed. As a result, the regions of relatively high values of $|\tau|/\tau_m$ are confined to the sides of the cylinder in the KC = 1.5, $U_s' = 0$ simulation, as observed in Fig. 13(a) that shows the bed shear stress distribution at $t = T/4$ when the magnitude of the approaching flow is the largest. By contrast, the total size of the regions where $|\tau|/\tau_m > 1.3$ in the KC = 30.8, $U_s' = 0$ simulation [Fig. 13(b)] is about 7 times larger at $= T/4$ mainly due to the presence of large billow vortices around the cylinder. The contribution of the HV vortex to the amplification of the bed shear stress is relatively low at $t = T/4$ in the KC = 30.8, $U_s' = 0.0$ simulation, which confirms that for such cases most of the sediment entrainment is due to the vortices shed from the cylinder. As the steady current component in the low KC number simulations becomes comparable to, or larger than, U_m, pair of symmetric vortices are shed on the downstream side (see Sec. III A). For $U_s' \geqslant 1$, these wake vortices together with the main HV drive the amplification of the bed shear stress around the cylinder over most of the oscillatory cycle [e.g., see results at $t = 3T/4$ in Figs. 14, 6(b), and 3] except at times when the magnitude of the incoming flow is close its peak [e.g., see results at $t = T/4$ for the KC = 1.5, $U_s' = 1.0$ simulation in Fig. 13(c)]. Around $t = T/4$, the bed shear stress distributions near the cylinder in the low KC number cases with $U_s' \geqslant 1.0$ are qualitatively similar to those in the corresponding purely oscillatory case [Fig. 13(a)]. The larger amplification of the bed shear stress on the sides of the cylinder in the KC = 1.5 $U_s' = 1.0$ case [Fig. 13(c)] compared to the KC = 1.5 $U_s' = 0$ case [Fig. 13(a)] is due to the shedding of a pair of symmetric

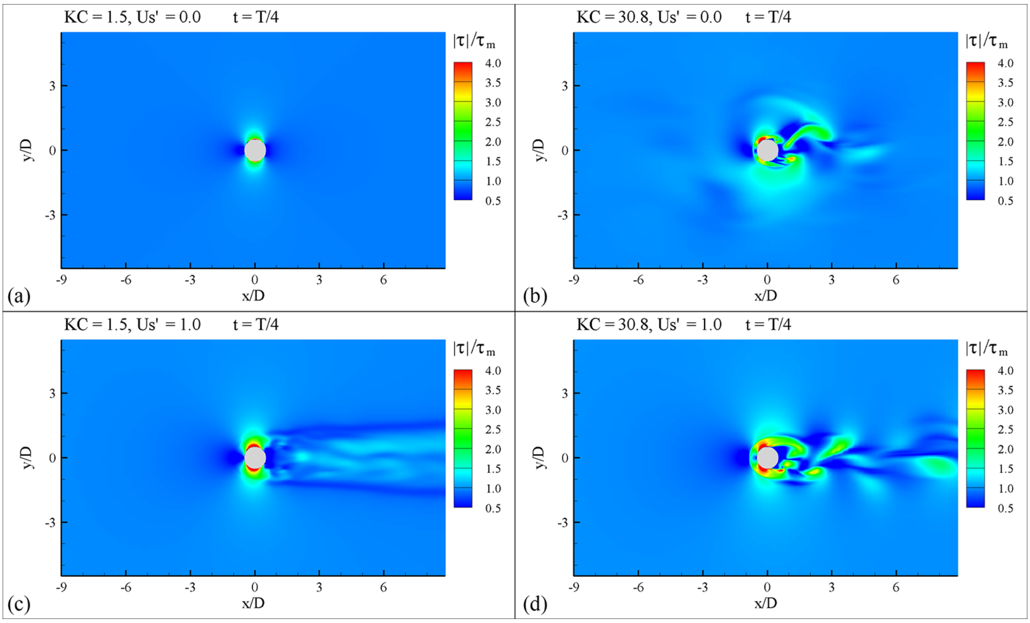

FIG. 13. Nondimensional bed shear stresses magnitude $|\tau|/\tau_m$ at $t = T/4$ in the KC = 1.5 and KC = 30.8 simulations. (a) KC = 1.5 and $U_s' = 0.0$; (b) KC = 30.8 and $U_s' = 0.0$; (c) KC = 1.5 and $U_s' = 1.0$; (d) KC = 30.8 and $U_s' = 1.0$.

vortices in the former case that remain for a long time in the vicinity of the cylinder [DV1 in Fig. 6(b)].

B. Bed shear stress distributions along the symmetry plane

Figure 15 gives more details on the erosive potential of the flow on the upstream side ($x/D < 0$) of the cylinder where HVs are sometimes present. The distributions of $\bar{\tau}/\tau_m$ are plotted at $t = T/4$ when the magnitude of the incoming flow is the largest. This is also the time when the largest negative values of the bed shear stress around the upstream face of the cylinder are recorded. The reduction of the bed shear stress near the cylinder is related to the deceleration of the incoming flow. Additionally, the presence of negative values of the bed shear stress near the cylinder in some of the simulations is directly related to the presence of a sufficiently strong downflow parallel to the upstream face of the cylinder. As the downflow approaches the bed, it has to move parallel to

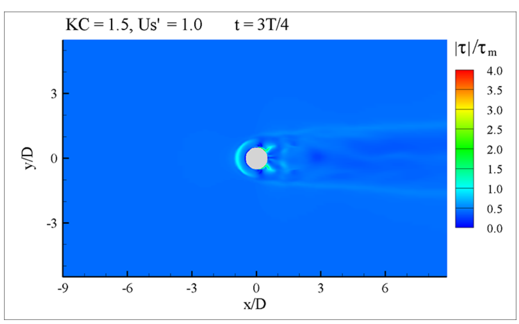

FIG. 14. Nondimensional bed shear stresses magnitude $|\tau|/\tau_m$ at $t = 3T/4$ in the KC = 1.5, $U_s' = 1.0$ simulation.

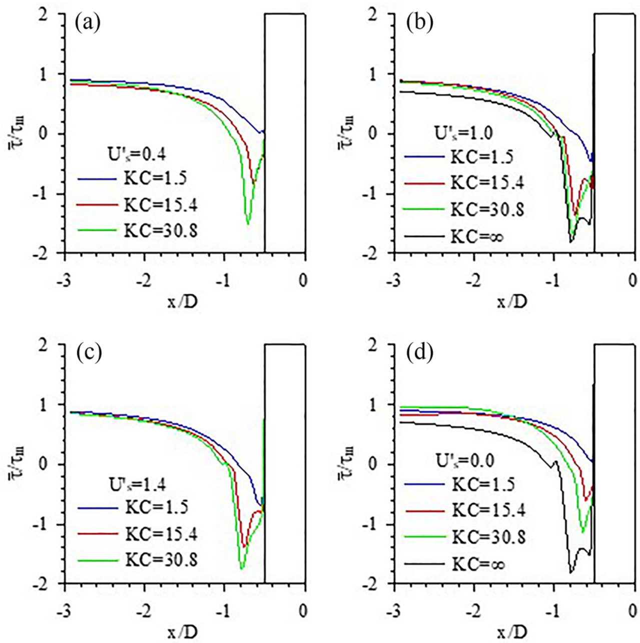

FIG. 15. Nondimensional, phase-averaged bed shear stress, $\bar{\tau}/\tau_m$, in the symmetry ($y/D = 0$) plane at $t = T/4$. (a) $U_s' = 0.4$; (b) $U_s' = 1.0$; (c) $U_s' = 1.4$; (d) $U_s' = 0$. Also included in panels (b) and (d) are results for a steady current simulation conducted with $U_s = U_m$.

the bed and away from the cylinder. For a sufficiently strong downflow, one or multiple corotating horseshoe vortices form and their direction of rotation is such that they advect near-bed fluid away from the cylinder (e.g., in the negative streamwise direction). These results are consistent with the experimental observations of [19].

In the high KC number cases, the capacity of the HVs to induce large bed shear stresses is also the largest around $t = T/4$. Though the size of the core of the main HV is not the largest at $t \approx T/4$ (e.g., see Fig. 10), its circulation is high and the vortex is situated in the immediate vicinity of the bed. No HV is present at $t = T/4$ in the KC = 1.5, $U_s' = 0.4$ and KC = 1.5, $U_s' = 0$ cases, consistent with the fact that $\bar{\tau}/\tau_m$ approaches zero near the face of the cylinder without becoming negative [Figs. 15(a) and 15(d)]. Even at $t = 3T/4$ when a HV is present in the KC = 1.5, $U_s' = 0.4$ case, there is no clear amplification of $\bar{\tau}/\tau_m$ near the front face of the cylinder.

For a fixed U_s', the erosive potential of the flow in front of the cylinder measured by the magnitude of the bed shear stress in that region increases monotonically with the KC number, though the rate of increase is not uniform (Fig. 15). This effect is mainly due to the increase in the circulation and lifetime of the HVs with increasing KC number [see Sec. III B and Fig. 9(a)]. As opposed to the low KC number simulation with $U_s' = 0.4$, where the magnitude of the phase-averaged shear stress is close to zero, large negative values of $\bar{\tau}/\tau_m$ are induced close to the upstream face of the cylinder, beneath the core of the horseshoe vortex, in the corresponding high KC number simulations [Fig. 15(a)]. For KC = 30.8, the magnitude of the peak nondimensional bed shear stress is larger than one, so the erosive capability of the HV is larger compared to that of the approaching flow. This trend is even stronger in the high KC number simulations performed with $U_s' = 1.0$ where the peak magnitude of $\bar{\tau}/\tau_m$ in the KC = 30.8 simulation is close to 1.8. One should also note that this value is very close to the peak value obtained for a steady current simulation conducted with the same U_s as in the $U_s' = 1$ combined wave-current simulations. The only qualitative difference between the distribution of the bed shear stress in the steady and the KC = 30.8 simulations is the presence of

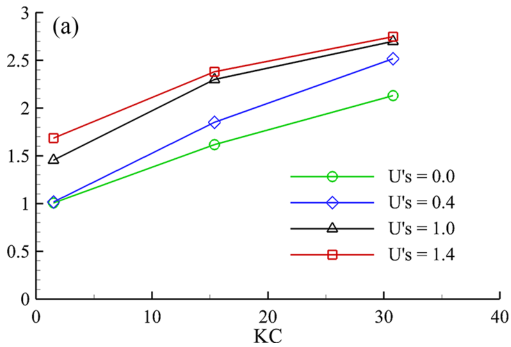

FIG. 16. Peak reduction of the nondimensional phase-averaged bed shear stress in the symmetry plane ($y/D = 0$) at $t = T/4$ with respect to the value in the undisturbed flow at $t = T/4$. (a) $|\bar{\tau}_{\min} - \tau_m|/\tau_m$ vs the KC number for constant U_s'; (b) $|\bar{\tau}_{\min} - \tau_m|/\tau_m$ vs U_s' for constant KC number.

a second peak close to the cylinder's face in the steady simulation due to a fairly strong junction vortex forming near the base of the cylinder. So, for sufficiently high KC numbers, the peak erosive capability of the main HV during the oscillatory cycle in combined wave-current flow is about the same as the one of the main HV in steady current flow. One should also note that the peak value of $\bar{\tau}/\tau_m$ does not increase in the $U_s' = 1.4$ simulations [Fig. 15(c)] that show a similar trend with increasing KC number. The only qualitative difference between the variations of $\bar{\tau}/\tau_m$ in front of the cylinder in the KC = 15.4 and KC = 30.8 simulations with $U_s' \geqslant 1.0$ [Figs. 15(b) and 15(c)] is the presence in the KC = 15.4 simulations of a second region of amplified negative bed shear stress very close to the cylinder. This second peak is induced by a secondary HV that is characterized by a higher peak circulation in the KC = 15.4 simulations. It is also relevant to analyse similar results for the purely oscillatory cases [Fig. 15(d)]. The magnitude of the peak value of $\bar{\tau}/\tau_m$ is larger than one only in the KC = 30.8 simulation. This value remains much lower than the peak value predicted in a steady current simulation with the incoming velocity equal to the maximum of the oscillatory streamwise velocity in the approaching flow.

Figure 16 summarizes the aforementioned trends in the amplification of the erosive potential of the flow in front of the cylinder as a result of increasing the KC number. The quantity plotted in Fig. 16 is $|\bar{\tau}_{\min} - \tau_m|/\tau_m$ where $\bar{\tau}_{\min}$ corresponds to the peak negative value of the phase-averaged bed shear stress in Fig. 15. A value of one means no erosion can occur. Values larger than two mean that the erosive capability of the flow is larger than that at large distances from the cylinder. In a good approximation, these values are fairly independent of U_s' for $U_s' \geqslant 1$.

Given that τ_m varies significantly with U_s', a more relevant comparison of the variation of the erosive capability of the flow in front of the cylinder with increasing U_s' is to compare the distributions of $\bar{\tau}/\rho U_m^2$. For both low and high values of the KC number, the peak magnitude of $\bar{\tau}/\rho U_m^2$ in front of the cylinder increases monotonically with U_s' (Fig. 17). The main trends can be also inferred from Fig. 16(b) that shows the variation of $|\bar{\tau}_{\min} - \tau_m|/\tau_m$ with U_s' for constant KC number. In particular, the effect of increasing U_s' is the same in the simulations conducted with KC = 15.4 [Fig. 17(b)] and KC = 30.8 [Fig. 17(c)] though the values of $|\bar{\tau}_{\min} - \tau_m|/\tau_m$ are consistently higher in the KC = 30.8 simulations. It is expected the rate of increase is going to approach zero for KC numbers much larger than 30. The monotonic of $|\bar{\tau}_{\min} - \tau_m|/\tau_m$ with U_s' for KC = 30.8 is consistent with the increase of the circulation of the main HV at $t = T/4$ observed in Fig. 9(b).

C. Implications for sediment erosion potential of the flow and scour

A main difference between the sediment erosion potential of the flow in the purely oscillatory cases and in the combined wave-current flow cases with $U_s' \geqslant 0.4$ is that the levels of $\bar{\tau}/\tau_m$ around

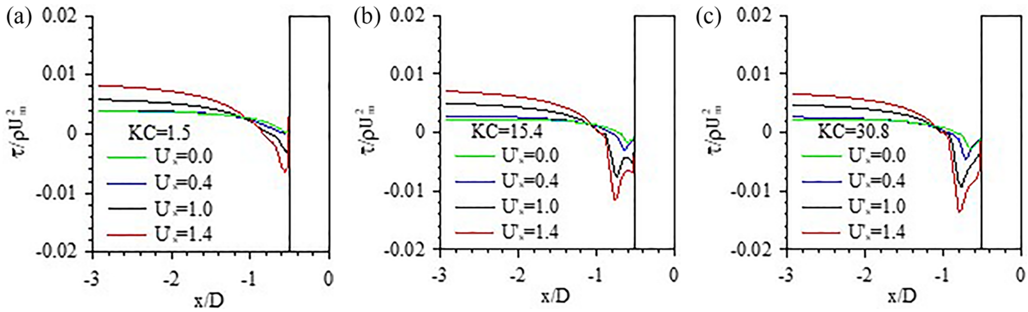

FIG. 17. Nondimensional, phase-averaged bed shear stress, $\bar{\tau}/\rho U_m^2$, in the symmetry ($y/D = 0$) plane at $t = T/4$. (a) KC = 1.5; (b) KC = 15.14; (c) KC = 30.8.

the cylinder are much larger over the first half period compared to the second half period when the magnitude of the approaching flow is generally smaller. This effect is illustrated for the KC = 30.8, $U_s' = 0.4$ case in Fig. 11(a) that shows the bed shear stress distributions at $t = 3T/8$ during the first half of the oscillatory cycle and at $t = 3T/4$ during the time when the approaching flow changes direction. Analysis of the bed shear stress distributions during the whole oscillatory cycle has shown this is a general characteristic of these flows. So, for both the low and the high KC number values considered in this study, the sediment erosion potential of the flow is much larger over the half cycle the steady component is oriented in the same direction as the oscillatory component if $U_s' \geqslant 0.4$.

Comparison of the bed shear stress distributions during the oscillatory cycle also suggest that for simulations conducted with a constant value of U_s' larger than 0.4, the sediment erosion potential of the flow increases monotonically with increasing KC number. Assuming the erosive potential of the flow near the cylinder at the start of the erosion-deposition process is an indicator of the magnitude of the scour at equilibrium, this result is consistent with the observed increase of the maximum scour depth with the KC number for constant U_s', or equivalently for a constant value of the combined wave-current parameter $U_s/(U_s + U_m)$, in the movable bed experiments ($4 < \mathrm{KC} < 26$) with codirectional wave and current conducted by [40]. This effect is stronger for small values of $U_s' = U_s/U_m$ and $U_s/(U_s + U_m)$ in the experiments which is consistent with the observed variation of the erosive potential of the flow near the upstream face of the cylinder in the present simulations. Results in Fig. 16(a) for the mixed wave current cases show that the rate of increase of $|\bar{\tau}_{\min} - \tau_m|/\tau_m$ with KC is largest in the simulations conducted with $U_s' = 0.4$ and the smallest in the simulations conducted with $U_s' = 1.4$. Results in Fig. 15 also show that for KC = 30.8 and $U_s' \geqslant 1.0$, the peak bed shear stress near the upstream face of the cylinder is only slightly smaller than the value in the corresponding steady current simulation. This finding is consistent with the experiments of [40] that found the maximum scour hole in experiments performed with KC = 26 and $U_s/(U_s + U_m) > 0.5$ ($U_s' \geqslant 1.0$) was less than 10% smaller than the predicted value in the steady current experiment.

The monotonic increase of the sediment erosion potential of the flow with the KC number predicted in the combined wave-current cases is not observed in the purely oscillatory flow cases where [17] found the sediment erosion potential of the flow peaks for KC = 15.4. However, that was mostly due to the presence of large cycle-to-cycle variations in the dynamics and coherence of the wake billow vortices, something never observed in the present mixed wave-current flow simulations. In the simulations with $U_s' \geqslant 0.4$ the increase in the bed shear stress levels with increasing KC number is mainly driven by the enhanced erosion potential of the HV system forming around the upstream face of the cylinder. This finding is consistent with the fact that, the lifespan of the main HV, its circulation and its capacity to amplify the bed shear stress are increasing with the KC number for constant U_s'.

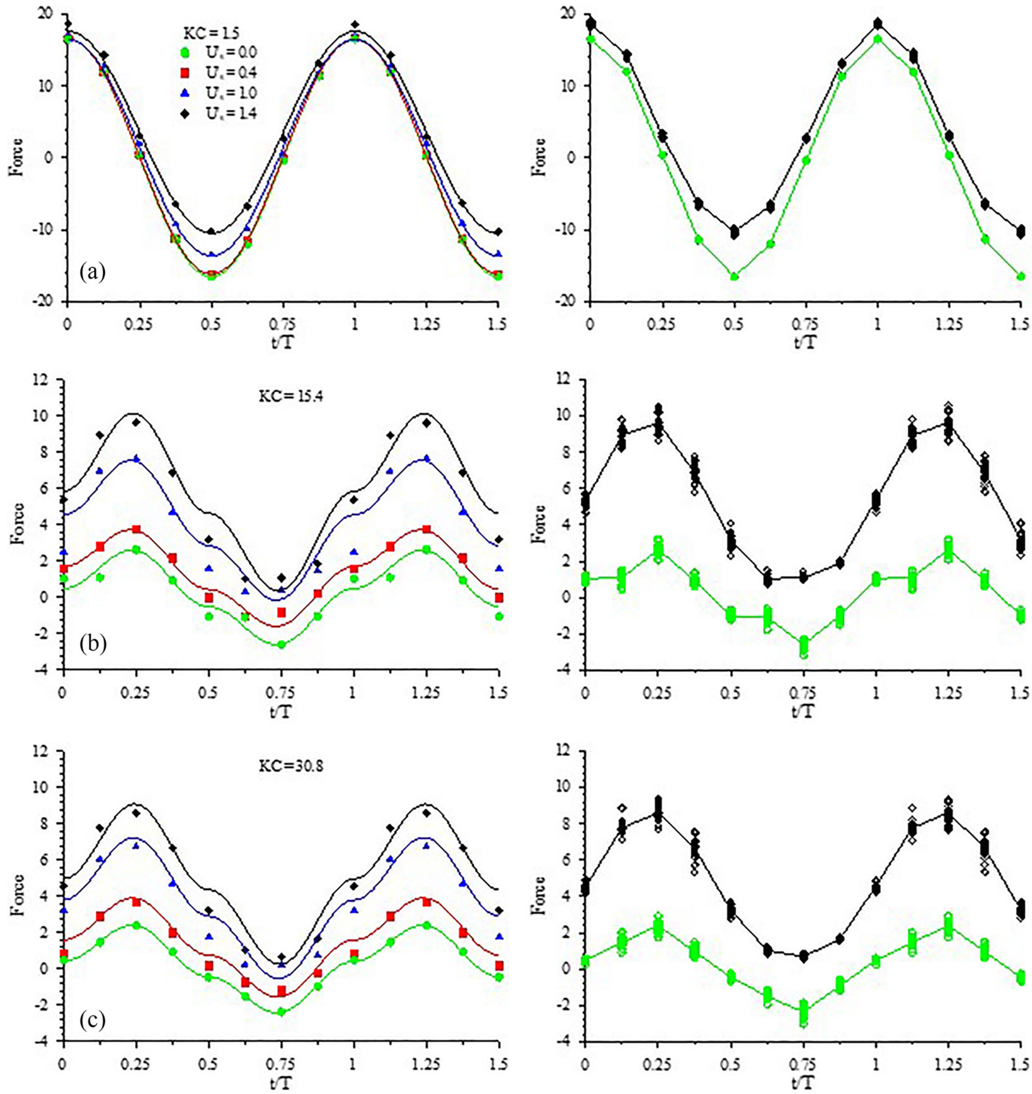

FIG. 18. Nondimensional (streamwise) in-line force vs nondimensional time, t/T. (a) KC = 1.5; (b) KC = 15.4; (c) KC = 30.8. The solid symbols in the left panels show the values of the phase-averaged in-line force, $\overline{F_x'}$. The solid lines in the left panels show $\overline{F_{xs}'} + \overline{F_{IF}'}$ where $\overline{F_{IF}'}$ is the oscillatory component of $\overline{F_x'}$ predicted using Morrison's equation and $\overline{F_{xs}'}$ is the mean (cycle-averaged) in-line force. The open symbols in the right panels show the instantaneous in-line force, F_x', for each oscillatory cycle (n = 1 to 20). The solid lines in the right panels show $\overline{F_x'}$.

V. FORCES ACTING ON THE CYLINDER

The phase-averaged, nondimensional streamwise (in-line), and spanwise (lift) forces acting on the solid cylinder, $\overline{F_x'}(t/T) = \overline{F_x}/(0.5\rho U_a^2 DH)$ and $\overline{F_y'}(t/T) = \overline{F_y}/(0.5\rho U_a^2 DH)$ are compared in Figs. 18 and 20 while the standard deviation of the nondimensional streamwise force acting on the cylinder is shown in Fig. 19. In general, a prime symbol is used to denote a force that was normalized by $0.5\rho U_a^2 DH$, where $U_a = 0.622\ U_m$ is the mean value of the oscillatory component of $\hat{u}$ over one half cycle, same for all simulations. The phase-averaging was conducted over 20 oscillatory cycles.

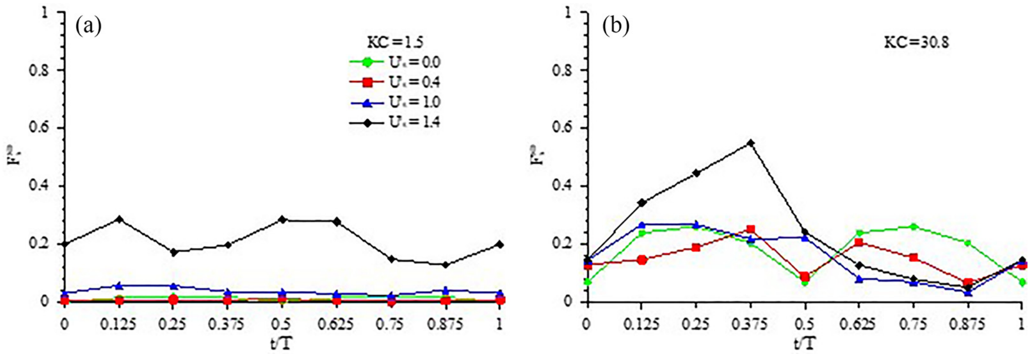

FIG. 19. Standard deviation of the nondimensional in-line force acting on the cylinder, $F_x^{\prime SD}$ vs nondimensional time, t/T. (a) KC = 1.5; (b) KC = 30.8.

Some of the plots in Figs. 18 and 20 also include the nondimensional forces over the individual cycles, $F_x^{'}(t/T)$ and $F_y^{'}$(t/T).

Chang and Constantinescu [17] found that the equation proposed by [27] to estimate the phase-averaged in-line force per unit length on a long cylinder placed in oscillatory flow gives fairly accurate predictions of the in-line force acting on a vertical cylinder placed in a depth-limited flow with a boundary layer developing over the bottom surface. In the present paper, we investigate if the same equation can be used to approximate the oscillatory component, $\overline{F}_{xo}$, of the phase-averaged in-line force, $\overline{F_x}$, for cylinders placed in mixed wave-current flows. For such cases, the velocity used in the equation corresponds to the purely oscillatory far-field component $\hat{u}_0$, where $\hat{u} = U_s + \hat{u}_0$, or equivalently, $\hat{u}' = U_s' + \hat{u}_0'$. In the present simulations, $\hat{u}_0 = U_m \sin(2\pi t/T)$. The expression of the nondimensional, phase-averaged in-line force predicted by Morrison's equation, $\overline{F_{IF}^{'}}(t/T)$, is

$$\overline{F_{IF}^{'}} = C_m \frac{\pi}{4} \frac{D}{TU_a^2} \frac{\partial \hat{u}_o}{\partial\left(\frac{t}{T}\right)} + C_d \frac{1}{2} \frac{\hat{u}_o|\hat{u}_o|}{U_a^2} = C_m \frac{\pi}{4} \frac{1}{0.622^2 KC} \frac{\partial \hat{u}_0'}{\partial\left(\frac{t}{T}\right)} + C_d \frac{1}{2} \frac{\hat{u}_0'|\hat{u}_0'|}{0.622^2}, \tag{3}$$

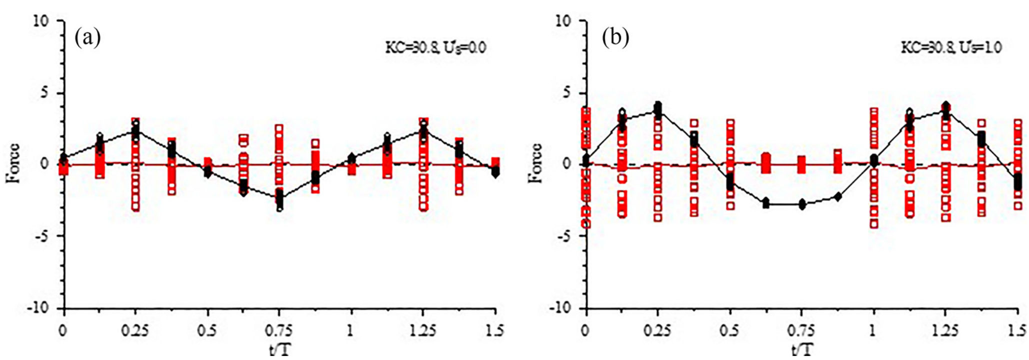

FIG. 20. Nondimensional spanwise force vs nondimensional time, t/T in the KC = 30.8 simulations. (a) $U_s' = 0$; (b) $U_s' = 1.0$. The open red symbols show the instantaneous spanwise force, $F_y^{'}$, for each oscillatory cycle ($n = 1$ to 20). The phase-averaged spanwise force, $\overline{F_y^{'}}$, is shown using a red solid line. Also shown are $F_{xo}^{'}$ (open black symbols) and $\overline{F_{xo}^{'}}$ (solid black line).

TABLE II. Nondimensional variables characterizing the in-line forces acting on the cylinder for the test cases.

KC	U_s'	C1	C2	C_m	C_d	$\overline{F}_{\text{xmax}}/(\rho U_m^2 DH)$	$\overline{F}_{\text{xmax}}/(0.5\rho U_{as}^2 DH)$	$\overline{F_x'}^{\text{rms}}$	C_{Fx}^{rms}	$\overline{F_{xs}'}$	C_{ds}
1.5	0.0	16.5	0	1.94	0	3.2	16.5	11.72	20.4	0	—
1.5	0.4	16.37	0	1.93	0	3.21	6.46	11.62	20.2	0.18	0.44
1.5	1.0	15.11	0	1.78	0	3.29	2.7	10.96	19.1	1.42	0.55
1.5	1.4	14.09	0	1.66	0	3.62	1.92	10.82	18.8	3.58	0.71
15.4	0.0	0.5	2.44	0.65	1.89	0.70	3.6	1.59	276.8	0	—
15.4	0.4	0.63	2.62	0.74	2.03	0.73	1.46	1.96	341.9	1.08	2.61
15.4	1.0	0.85	3.81	1.00	2.95	1.49	1.22	4.20	730.9	3.21	1.24
15.4	1.4	0.61	4.88	0.72	3.78	1.86	1.0	5.76	1002.5	4.76	0.94
30.8	0.0	0.5	2.0	1.17	1.54	0.58	3.0	1.50	1044.6	0	–
30.8	0.4	0.42	2.72	0.99	2.10	0.71	1.42	1.89	1316.9	0.93	2.25
30.8	1.0	0.45	3.87	1.06	2.99	1.30	1.06	3.85	2681.1	2.97	1.15
30.8	1.4	0.3	4.41	0.71	3.41	1.67	0.88	5.18	3610.1	4.28	0.84

where C_m and C_d are the inertia and drag coefficients, respectively, and $\overline{F_{IF}'}$ is used to approximate $\overline{F_{xo}'}$. Using the expression for $\hat{u}_0'$, Eq. (3) can be written as

$$\overline{F_{IF}'} = C_1 \cos\left(2\pi\frac{t}{T}\right) + C_2 \sin\left(2\pi\frac{t}{T}\right)\left|\sin\left(2\pi\frac{t}{T}\right)\right|. \tag{4}$$

Once $\overline{F_x'}$ is split into its steady and oscillatory components,

$$\overline{F'_x} = \overline{F'_{xs}} + \overline{F'_{xo}}, \tag{5}$$

the steady component $\overline{F}_{xs}$ (e.g., the average value of $\overline{F_x}$ over the whole oscillatory cycle) can be easily estimated and a best-fit procedure can be used to determine the constants C_1 and C_2 in Eq. (4) and then C_m and C_d in Eq.. (3). For the mixed wave-current flow cases, one can use the steady current velocity, U_s, to define a drag coefficient, C_{ds}, for the steady component of the phase-averaged in-line force such that

$$\overline{F}_{xs} = 0.5 C_{\text{ds}} \rho U_s^2 DH. \tag{6}$$

As was also the case for purely oscillatory flow, the temporal variation of $\overline{F_x}$ is close to a cosine function in the KC = 1.5 simulations conducted with $0.4 \leqslant U_s' \leqslant 1.4$ [Fig. 18(a)]. Consistent with this, the estimated values of C_2 and C_{d} in Eqs. (3) and (4) are equal to zero for all KC = 1.5 simulations (Table II). Given that the variation of $\hat{u}$ is sinusoidal, the in-line force is out-of-phase with the velocity in the far field flow for low KC numbers. So, for such cases the in-line force is due only to inertia effects, which is consistent with the purely oscillatory flow experiments of [20] that found $C_m \approx 2.0$ and $C_{\text{d}} = 0$ for very low KC numbers.

In the KC = 1.5 simulations, the amplitude of the oscillatory component, $\overline{F}_{xo}$, decreases slightly with increasing U_s'. This is confirmed in a quantitative way by the variation of the root-mean-square (r.m.s.) of the nondimensional in-line forces over the whole oscillatory cycle, $\overline{F_x'}^{\text{rms}}$, also included in Table II. Consistent with the observed trends in the variations of $\overline{F}_{xo}$ and $\overline{F_x'}^{\text{rms}}$, the inertia coefficient C_m decreases with U_s' [Fig. 18(a) and Table II]. The peak (phase-averaged) in-line force over the cycle $\overline{F}_{\text{xmax}}$ increases with U_s' [see Fig. 18(a) and Table II where, following [20], $\overline{F}_{\text{xmax}}$ is nondimensionalized using U_m rather than U_{a}] because of the increase of the component of the-line force associated with the steady current component, $\overline{F_{xs}'}$ (Table II). As $\overline{F}_{\text{xmax}}$ is reached at $t = 0$ and $t = T$, the phase angle corresponding to the maximum in-line force is equal to zero in the KC = 1.5 cases. Regardless of the value of U_s', the variation of the instantaneous in-line force, F_x', over each cycle remains very close to that of $\overline{F_x'}$ [Fig. 18(a)]. This information is presented in a more quantitative way in Fig. 19(a) that shows the temporal variation of the standard deviation of the in-line force, $F_x^{\prime SD}$. In a good approximation, $F_x^{\prime SD} \approx 0$ for $U_s' \leqslant 1.0$, while $F_x^{\prime SD} \approx 0.25$ in the KC $= 1.5$, $U_s' = 1.4$ case.

The temporal variation of $\overline{F'}_x$ is more complex in the high KC number simulations [Figs. 18(b) and 18(c)]. Regardless of the value of U_s', the peak values of $\overline{F'}_x$ occur for a phase angle of 90 degrees ($t = T/4$) in the KC $= 15.4$ and KC $= 30.8$ simulations. Due to the steady current component, the magnitude of $\overline{F'}_x$ is smaller at $t = 3T/4$ than at $t = T/4$ for $U_s' > 0$. As opposed to the low KC number simulations, the amplitude of $\overline{F}_{xo}$ increases monotonically with U_s' (see also $\overline{F_x'}^{\mathrm{rms}}$ in Table II) and fairly large, cycle-to-cycle variations of F'_x are observed for KC $\geqslant 15.4$. Given that $\overline{F_{xs}'}$ also increases with U_s', the rate of increase of $\overline{F}_{\mathrm{xmax}}$ with U_s' is larger in the high KC number simulations. One interesting result is that for constant U_s', the steady component, $\overline{F_{xs}'}$, decays slightly with increasing KC number (Table II). For all cases, $\overline{F_{IF}'} + \overline{F_{xs}'}$ approximate reasonably well $\overline{F'}_x$ over the whole oscillatory cycle [Figs. 18(b) and 18(c)].

Chang and Constantinescu [17] have shown that the predicted values of C_m and C_d for the purely oscillatory cases (Table II) are fairly close to those inferred from experiments (see Figs. 10 and 11 in [20]). For constant KC number, the drag term contribution and the drag coefficient C_d (Table II) increase monotonically with the magnitude of the steady current component. Meanwhile, the inertia coefficient C_m peaks for $U_s' = 1$ before starting decaying for $U_s' > 1$. Though for fixed KC number, $\overline{F}_{\mathrm{xmax}}$ increases with U_s' [e.g., see $\overline{F}_{\mathrm{xmax}}/(\rho U_m^2 \mathrm{DH})$ in Table II, where U_m is the same in all simulations], it is also of interest to investigate how $\overline{F}_{\mathrm{xmax}}$ varies when nondimensionalized using a velocity scale which accounts for the fact that the cylinder is placed in a mixed wave-current flow. Such a velocity scale is $U_{\mathrm{as}} = 0.622U_m + U_s$. For a constant KC number, $\overline{F}_{\mathrm{xmax}}/(0.5\rho U_{as}^2 \mathrm{DH})$ decreases monotonically with increasing U_s' (Table II).

As opposed to what was observed in the KC $= 1.5$ simulations, the cycle-to-cycle variations of $\overline{F'}_x$ are non-negligible for all values of U_s' in the KC $= 15.4$ [Fig. 18(b)] and KC $= 30.8$ [Fig. 18(c)] simulations. For $U_s' > 0$, higher values of $F_x^{\prime SD}$ are generally observed over the first half of the cycle when the oscillatory flow velocity component is oriented in the same direction as the steady current velocity [e.g., see Fig. 19(b) for KC $= 30.8$]. As for the KC $= 1.5$ simulations, a strong increase in the peak value of $F_x^{\prime SD}$ is observed in the $U_s' = 1.4$ simulations conducted with KC $= 15.4$ and KC $= 30.8$ where the peak values of $F_x^{\prime SD}$ are around 0.6 [Fig. 19(b)].

Following [26], the variation of $\overline{F'}_x^{\mathrm{rms}}$ with the KC number and U_s' is also reported in Table II in the form of a force coefficient, C_{Fx}^{rms}, where the force acting on the whole cylinder is nondimensionalized by $(\frac{1}{2}\rho\frac{D^2}{T^2})DH = \frac{1}{2}\rho\frac{U_m^2}{KC^2}DH$. Chang and Constantinescu [17] found that the estimated values of C_{Fx}^{rms} for the purely oscillatory cases were in fairly good agreement with the values obtained using the empirical formula proposed by [26], $C_{Fx}^{\mathrm{rms}} = (160.\mathrm{KC}^2 + 0.69.\mathrm{KC}^4)^{0.5}$. This formula provides an upper bound for C_{Fx}^{rms} in the low KC number cases with combined wave-current flow (Table II). However, the high KC number cases are characterized by a strong nonlinear increase of C_{Fx}^{rms} with U_s'.

We already commented on how the steady component of the in-line force, $\overline{F_{xs}'}$, varies with the KC number and U_s'. For the simulations conducted with a nonzero steady current, Table II also reports the values of the drag coefficient, C_{ds}, defined by Eq. (6). While in the low KC number simulations C_{ds} increases with U_s', the opposite is true for the high KC number simulations. The values of this drag coefficient are 0.84 and 0.94 in the KC $= 15.4$ and KC $= 30.8$ simulations performed with $U_s' = 1.4$. A steady current simulation performed with $\mathrm{Re}_s \approx 150\,000$ in the same domain predicted a drag coefficient of 0.85. This value is typical for finite-length cylinders placed in an open channel flow where the presence of the channel bottom and associated boundary layer result is a decay of the drag coefficient compared to standard values reported for long cylinders (e.g., see [12]). This suggests that, for high KC number mixed wave-current flows and $U_s \gg U_m$, one can estimate the steady component of the phase-averaged in-line force using Eq. (6) with the drag coefficient obtained for the corresponding case of steady current (no wave component) flow.

For KC = 1.5, the phase-averaged spanwise force, $\overline{F_y'}(t/T)$, has negligible values not only in the simulation with purely oscillatory flow, where no billow vortices are shed during the oscillatory cycle, but also in the mixed wave-current simulations where such vortices form. Except for the KC = 15.4, $U_s' = 0$ case, where the number of shed vortices during each oscillatory cycle is not always the same, the values of $\overline{F'_y}$ remain low in the high KC number simulations, too. However, the presence of negligible spanwise forces in the phase-averaged flow does not mean the cylinder is not subject to large spanwise forces in the instantaneous flow fields. This finding is exemplified in Figs. 20(a) and 20(b) for the KC = 30.8 simulations with $U_s' = 0$ and $U_s' = 1.0$, respectively, where the values of F'_y during the various cycles are included together with $\overline{F'_y}$. The trends are similar for $U_s' = 0.4$ and $U_s' = 1.4$. For purely oscillatory flow, the largest cycle-to-cycle variations of F'_y are recorded around $t = T/4$ and $t = 3T/4$ [e.g., see Fig. 20(a)], when the magnitude of the far-field velocity is the largest. Meanwhile, for relatively large values of the steady current component (e.g., for $U_s' \geqslant 1.0$), large values of F'_y are observed over the first half of the oscillatory cycle [$0 < t < T/2$, see Fig. 20(b)]. These forces are induced by the vertical vortex tubes and wake billow vortices moving close to the sides of the cylinder or separating from it. Meanwhile, F'_y remains very low for $T/2 < t < T$ [e.g., see Fig. 20(b)] when the steady flow and oscillatory flow velocity components have opposite signs. However, regardless of the value of U_s', the maximum values of F'_y are comparable not only to the peak values of the phase-averaged in-line force but even to the peak values of F'_x. So, a cylinder placed in a mixed wave-current flow at high KC numbers can be, at times, subject to comparable instantaneous forces along the streamwise and spanwise directions, even though the phase-averaged spanwise forces are very low and the forcing flow is oriented along the streamwise direction.

Figures 21(a) and 21(b) compare the phase-averaged in-line force coefficient for the cylinder, $\overline{C}_{Fx} = \frac{\overline{F_x}}{0.5\rho\hat{u}^2(t)DH}$, during the oscillatory cycle for simulations performed with KC = 15.4 and KC = 30.8, respectively. This coefficient is formally identical to the standard streamwise drag coefficient defined in steady flow past cylinders. As already discussed, the estimated drag coefficient from a steady current simulation performed in the same domain at $\mathrm{Re}_s = 150\,000$ was 0.85. In the purely oscillatory flow cases with KC = 15.4 and KC = 30.8, $\overline{C}_{Fx}$ varies between 0.8 and 1.1, except during short time intervals when $\hat{u}$ approaches zero during the oscillatory cycle. The cycle-averaged value of $\overline{C}_{Fx}$ for these cases is only about 10%–15% larger than the drag coefficient in steady flow assuming a channel velocity of $0.622U_m$.

Large periods of time during the oscillatory cycle when $\overline{C}_{Fx}$ is close to 0.85 are also predicted in the combined wave-current simulations with KC = 15.4 ($0.85 < \overline{C}_{Fx} < 1.0$) and KC = 30.8 ($0.6 < \overline{C}_{Fx} < 0.9$). As opposed to the purely oscillatory cases, values of $\overline{C}_{Fx}$ much larger than 1.0 are not related to $\hat{u}$ approaching zero. There is a qualitative change between cases with $U_s' = 0.4$, where $\overline{C}_{Fx} \gg 1$ over two time intervals in each cycle ($0.6T < t < 0.7T$ and $0.9 < t < 1.1T$), and cases with $U_s' \geqslant 1.0$ where $\overline{C}_{Fx} \gg 1$ over most of the second half of each cycle. The peak value of $\overline{C}_{Fx}$ over the oscillatory cycle decays significantly as U_s' increases from 1.0 to 1.4 for both KC = 15.4 and KC = 30.8 [Figs. 21(a) and 21(b)]. This suggests that as the steady current component becomes dominant (e.g., $U_s' \gg 1.0$), $\overline{C}_{Fx}$ will vary in a narrow range over the whole oscillatory cycle and the steady-current drag coefficient value will be within this range. Eventually, the main unsteadiness in $\overline{C}_{Fx}$ is going to be associated with the formation and shedding of vortices at the downstream side of the cylinder as for the case of a cylinder in steady current.

VI. SUMMARY AND CONCLUSIONS

Eddy resolving simulations revealed important differences in the flow structure between cases with a purely oscillatory flow ($U_s' = 0$) and cases when the cylinder was placed in combined wave-current flows ($U_s' \geqslant 0.4$) for both low KC numbers (oscillatory component does not induce the generation of wake vortices) and high KC numbers.

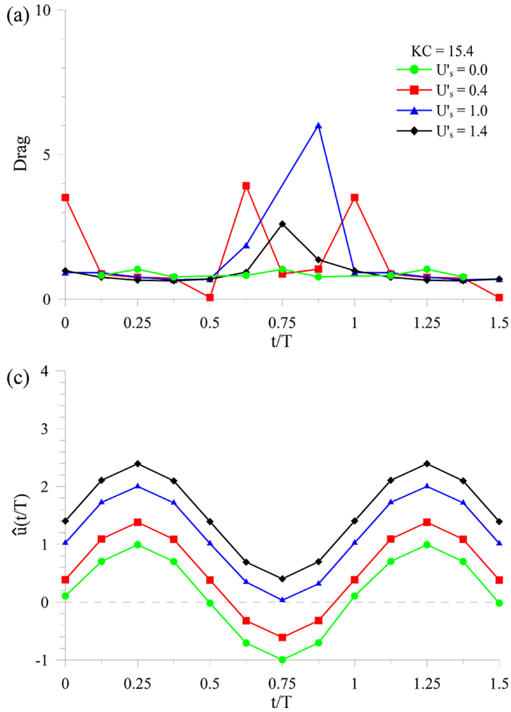

FIG. 21. In-line force coefficient vs nondimensional time, t/T. (a) KC = 15.4; (b) KC = 30.8. The open symbols show the phase-averaged in-line force coefficient, $\overline{C}_{Fx}$. To get the force coefficient, the in-line force is nondimensionalized with the depth-averaged streamwise velocity in the undisturbed flow $\hat{u}(t/T)$ shown in panel (c) and the projected area, HD. No values can be calculated when $\hat{u} = 0$.

The instantaneous and phase averaged flow fields allowed a detailed analysis of the vortices forming during the oscillatory cycle on both sides of the cylinder and an analysis of their dynamics, something that was not available from previous experimental and numerical studies of surface-mounted cylinders placed in a combined wave-current flow. The presence of a nonzero steady current component with $U_s' \geqslant 0.4$ in the simulations performed with KC $= 1.5$ led to a qualitative change in the wake flow with respect to the purely oscillatory flow case where no vortices are shed in the wake. The symmetric wake shedding mode dominated in all the combined wave-current flow simulations with two pairs of symmetric vortices shed each cycle on the downstream side of the cylinder for $U_s' = 0.4$ and only one for $U_s' = 1.0$ and $U_s' = 1.4$. The wake structure was very different in the high KC number cases where the antisymmetric wake shedding mode dominates in both the $U_s' = 0$ and the $U_s' \geqslant 0$ cases. For a constant value of the KC number, the number of antisymmetric vortices forming on the downstream side was larger in the $U_s' \geqslant 0$ cases compared to the corresponding $U_s' = 0$ case. Moreover, the number of shed vortices on the downstream side was found to generally increase with increasing U_s'. For example, in the KC = 30.8 simulations, the number of shed vortices on the downstream side was equal to six for $U_s' = 0.4$ and to eight for $U_s' = 1.0$ and 1.4. Moreover, the increase of U_s' was accompanied by a significant increase of the initial circulation of most of the shed vortices on the downstream side of the cylinder (e.g., of the order of 6 to 8 times if one compares results for $U_s' = 0.4$ and 1.4).

The present study also revealed that for low KC numbers a strong instability develops along the cores of the vortex tubes forming in the attached and separated shear layers in the combined wave-current simulations with $U_s' \approx 1.0$. This instability takes the form of an array of large-scale hairpin-like vortices and is induced by the presence of nearby vortex tubes of unequal size and circulation. This instability starts decaying once the steady current is sufficiently large for the flow to be unidirectional during the whole oscillatory cycle (e.g., $U_s' \gg 1$). This instability is not present for high KC numbers. The instability leading to the generation of near-bed horizontal vortices in the vicinity of the cores of the vertical wake billow vortices in the high KC number cases with purely oscillatory flow [17] was also found to be present in the corresponding combined wave-current flow cases. However, this instability becomes weaker for $U_s' > 1$. Most probably, this is related to the increased stretching of the cores of the main wake billow vortices near the bed surface with increasing U_s'.

Simulation results showed that for constant KC number, the erosive potential of the horseshoe vortices (HVs) on the upstream side of the cylinder increases with U_s, the opposite is true for the main HV on the downstream side and, more importantly, for the wake billow vortices. The decay of the erosive potential of the billow vortices is directly related to the aforementioned amplification of the stretching of the cores of these vortices as they interact with the bed. So, as U_s' increases, the scour around the cylinder is going to be driven primarily by the HVs on the upstream side and by the velocity amplification of the lateral sides of the cylinder rather than by the shed wake billows as is the case for the purely oscillatory flow cases. For a constant value of the steady flow component, the overall capacity of the HV on the upstream side of the cylinder to induce large bed shear stresses increases with the KC number.

While in the high KC number cases the capacity of the main HV to amplify the bed shear stress beneath its core always peaks at $t = T/4$, when the magnitude of the approaching flow is the largest, no main HV vortex is present around $t = T/4$ in some of the low KC number cases (e.g., in the KC = 1.5, $U_s' = 0.4$ case). For a constant value of the KC number, the lifespan of the main horseshoe vortex in each oscillatory cycle increases monotonically with U_s'. For high KC numbers, the main HV is present over the whole oscillatory cycle in the $U_s' = 1.4$ simulations. Moreover, the peak bed shear stress levels recorded beneath the HV vortex in the KC = 30.8, $U_s' = 1.0$ simulation were comparable to the mean peak value observed in a steady current simulation conducted with the same value of the steady component.

The presence of a nonzero steady current component did not affect the phase difference between the time the velocity in the far field flow peaks and the time the in-line force peaks. The amplitude of the oscillatory component of the phase-averaged in-line force was found to slightly decay with increasing U_s' for low KC numbers, while the opposite was true for high KC numbers. An important finding was that the oscillatory component of the phase-averaged in-line force variation over one oscillatory cycle can be reasonably well approximated by Morrison's equation proposed for long cylinders in purely oscillatory flow. For low KC numbers, the in-line force can be very well approximated by a cosine function for $0 \leqslant U_s' \leqslant 1.4$, which means that for such cases the in-line force is due only to inertia effects. At high KC numbers, the phase-averaged in-line force peaks at the time the far-field streamwise velocity reaches its maximum and drag component of the in-line force monotonically increases with U_s'. A drag coefficient can be introduced to scale the steady component of the in-line force using U_s as the velocity scale. A main finding of the present study is that for high KC numbers and high U_s', this drag coefficient approaches the value of the standard drag coefficient in steady current flow past the same cylinder.

While the phase-averaged spanwise force remained small during the oscillatory cycle in all high KC number simulations with $U_s' \geqslant 0.4$, the instantaneous spanwise force during some of the oscillatory cycle was, at times, as high as the highest values of the phase-averaged in-line force over the cycle. For $U_s' \geqslant 1$, large values of the instantaneous spanwise force were mostly observed for $0 < t < T/2$ when the oscillatory and steady flow components in the far field are in the same direction. Small spanwise forces were predicted for $T/2 < t < T$ over all cycles. This means that cylinders placed in combined wave-current flows are subject, at times, to comparable forces along the streamwise and spanwise directions if the KC number is high even though the far field flow is unidirectional. This finding has obvious consequences for strength and fatigue design of monopiles.

The present study considered simulations with moderate values of H/D. No qualitative changes in the flow physics are expected for cases with $H/D \gg 1$. Once flow shallowness effects become important, the number of shed vortices in each oscillatory cycle and the lifespan of the wake billow vortices are expected to decrease. Moreover, the dynamics of the main horseshoe vortex is also going to change as the size of its core becomes comparable to the flow depth. Based on steady current simulations [16], such effects are expected to become important for $H/D < 0.1$. The present approach can be used to investigate combined wave-current flows under shallow conditions. Future applications of interest (e.g., multiple-pile foundations, patches of vegetation) include cases where a circular array of solid cylinders is placed in combined wave-current flows. The present study can be thought as a limiting case for this type of applications where the solid volume fraction of the porous region containing the solid cylinders is equal to one.

ACKNOWLEDGMENT

We gratefully acknowledge the National Center for High-Performance Computing (NCHC) in Taiwan for providing the computational resources needed to conduct the simulations.

---

[1] T. U. Petersen, Scour around offshore wind turbine foundations, Ph.D. thesis, Department of Mechanical Engineering, Technical University of Denmark, 2014.
[2] H. Akilli and D. Rockwell, Vortex formation from a cylinder in shallow water, Phys. Fluids **14**, 2957 (2002).
[3] N. Apsilidis, P. Diplas, C. Dany, and P. Bouratsis, Time-resolved flow dynamics and Reynolds number effects at a wall–cylinder junction, J. Fluid Mech. **776**, 475 (2015).
[4] C. Baykal, D. Fuhrman, B. M. Sumer, N. G. Jacobsen, and J. Fredsøe, Numerical investigation of flow and scour around a vertical circular cylinder, Philos. Trans. R. Soc. A **373**, 20140104 (2015).
[5] C. Baykal, B. M. Sumer, D. Fuhrman, N. G. Jacobsen, and J. Fredsøe, Numerical simulation of scour and backfilling processes around a circular pile in waves, Coastal Eng. **122**, 87 (2017).
[6] Z. Cheng, M. Koken, and G. Constantinescu, Approximate methodology to account for effects of coherent structures on sediment entrainment in RANS simulations with a movable bed and applications to pier scour, Adv. Water Res. **120**, 65 (2018).
[7] Y. M. Chiew and B. Melville, Local scour around bridge piers, J. Hydraulic Res. **25**, 15 (1987).
[8] B. Dargahi, The turbulent flow field around a circular cylinder, Expts. Fluids **8**, 1 (1989).
[9] G. Kirkil, G. Constantinescu, and R. Ettema, DES investigation of turbulence and sediment transport at a circular pier with scour hole, J. Hydraul. Eng. **135**, 888 (2009).
[10] G. Kirkil and G. Constantinescu, Nature of flow and turbulence structure around an in-stream vertical plate in a shallow channel and the implications for sediment erosion, Water Resour. Res. **45**, W06412 (2009).
[11] G. Kirkil and G. Constantinescu, A numerical study of the laminar necklace vortex system and its effect on the wake for a circular cylinder, Phys. Fluids **24**, 073602 (2012).
[12] G. Kirkil and G. Constantinescu, Effects of cylinder Reynolds number on the turbulent horseshoe vortex system and near wake of a surface-mounted circular cylinder, Phys. Fluids **27**, 075102 (2015).
[13] W. G. Qi, J. Kiu, F. P. Gao, B. Li, and Q. G. Chen, Quantifying the spatiotemporal evolution of the turbulent horseshoe vortex in front of a vertical cylinder, Phys. Fluids **34**, 015110 (2022).
[14] A. Roulund, B. M. Sumer, J. Fredsøe, and J. Michelsen, Numerical and experimental investigation of flow and scour around a circular pile, J. Fluid Mech. **534**, 351 (2005).
[15] B. M. Sumer and J. Fredsøe, *Hydrodynamics Around Cylindrical Structures* (World Scientific, Singapore, 1997).
[16] J. Zeng and G. Constantinescu, Flow and coherent structures around circular cylinders in shallow water, Phys. Fluids **29**, 066601 (2017).
[17] W. Y. Chang and G. Constantinescu, Oscillatory flow around a vertical circular cylinder placed in an open

channel: Coherent structures, sediment entrainment potential and drag forces, J. Fluid Mech. **964**, A22 (2023).

[18] B. M. Sumer, J. Fredsøe, and N. Christiansen, Scour around a vertical pile in waves, J. Waterway Port Coastal Ocean Eng., **118**, 15 (1992).

[19] B. M. Sumer, N. Christiansen, and J. Fredsøe, The horseshoe vortex and vortex shedding around a vertical wall-mounted cylinder exposed to waves, J. Fluid Mech. **332**, 41 (1997).

[20] G. H. Keulegan and L. H. Carpenter, Forces on cylinders and plates in oscillating fluid, J. Res. Natl. Bureau Stand. **60**, 423 (1958).

[21] J. R. Elston, H. M. Blackburn, and J. Sheridan, The primary and secondary instabilities of flow generated by an oscillating circular cylinder, J. Fluid Mech. **550**, 359 (2006).

[22] E. D. Obasaju, P. W. Bearman, and J. M. R. Graham, A study of forces, circulation and patterns around a circular cylinder in oscillating flow, J. Fluid Mech. **196**, 467 (1988).

[23] T. Sarpkaya and M. Issacson, *Mechanics of Wave Forces on Offshore Structures* (Van Nostrand Reinhold, New York, 1981).

[24] M. Tatsuno and P. W. Bearman, A visual study of the flow around an oscillating circular cylinder at low Keulegan–Carpenter numbers and low Stokes numbers, J. Fluid Mech. **211**, 157 (1990).

[25] F. Tong, L. Cheng, C. Xiong, S. Draper, H. An, and X. Lou, Flow regimes for a square cross-section cylinder in oscillatory flow, J. Fluid Mech. **813**, 85 (2017).

[26] C. H. K. Williamson, Sinusoidal flow relative to circular cylinders, J. Fluid Mech. **155**, 141 (1985).

[27] J. R. Morrison, M. P. O'Brien, J. W. Johnson, and S. A. Schaaf, The forces exerted by surface waves on piles, J. Petrol. Tech. Am. Inst. Mining Energy **2**, 149 (1950).

[28] B. Chen and S. Li, Experimental study of local scour around a vertical cylinder under wave-only and combined wave-current conditions in a large-scale flume, J. Hydraulic Eng. **144**, 04018058 (2018).

[29] X. Deng, S. He, and Z. Cao, Numerical investigation of the local scour around a coconut tree root foundation under wave-current joint actions, Ocean Eng. **245**, 110563 (2022).

[30] R. W. Eadie and J. B. Herbich, Scour around a single, cylindrical pile due to combined random waves and a current, Coastal Eng. Proc. **136**, 1858 (1986).

[31] J. Li, B. Zhang, C. Shen, X. Fu, and W. Li, Experimental study on local scour depth around monopile foundation in combined waves and current, Sustainability **13**, 13614 (2021).

[32] X. Lyu, Y. Cheng, W. Wang, H. An, and Y. Li, Experimental study of local scour around submerged monopile under combined waves and current, Ocean Eng. **240**, 109929 (2021).

[33] M. C. Ong, D. Myrhaug, and P. Hesten, Scour around vertical piles due to long-crested and short-crested nonlinear random waves plus a current, Coastal Eng. **73**, 106 (2013).

[34] T. U. Petersen, B. M. Sumer, and J. Fredsøe, Time scale of scour around a pile in combined waves and current, *Sixth International Conference on Scour and Erosion* (ICSE, Paris, 2012).

[35] W. G. Qi and F. P. Gao, Equilibrium scour depth at offshore monopile foundation in combined waves and current, Sci. China Technolog. Sci. **57**, 1030 (2014).

[36] W. G. Qi and F. P. Gao, Physical modeling of local scour development around a large diameter monopile in combined waves and current, Coastal Eng. **83**, 72 (2014).

[37] M. Quezada, A. Tanburrino, and Y. Nino, Numerical study of the hydrodynamics of waves and currents and their effects on pier scouring, Water **11**, 2256 (2019).

[38] T. Raaijmakers and D. Rudolph, Time-dependent scour development under combined current and wave conditions–laboratory experiments with online monitoring technique, in *Fourth International Conference on Scour and Erosion* (Chuo University, Tokyo, 2008), pp. 152–161.

[39] A. Stahlmann, Numerical and experimental modelling of scour at foundation structures for offshore wind turbines, J. Ocean Wind Energy **1**, 82 (2014).

[40] B. M. Sumer and J. Fredsøe, Scour around a pile in combined waves and current, J. Hydraul. Eng. **127**, 403 (2001).

[41] M. Umeyama, Reynolds stress and velocity distributions in a wave-current coexisting environment, J. Waterways Port Coastal Ocean Eng. **131**, 203 (2005).

[42] M. Wu, L. De Vos, C. E. Arboleda, V. Stratigaki, T. Fazeres-Ferradosa, P. Rosa-Santos, F. Taveira-Pinto, and P. Troch, Large scale experimental study of the scour protection damage around a monopile foundation under combined wave and current conditions, J. Marine Sci. Eng. **8**, 417 (2020).
[43] C. J. Keylock, S. G. Constantinescu, and R. J. Hardy, The application of computational fluid dynamics to natural river channels: Eddy resolving versus mean flow approaches, Geomorphology **179**, 1 (2012).
[44] W. Y. Chang, G. Constantinescu, H. G. Lien, W. F. Tsai, J. S. Lai, and C. H. Loh, Flow structure around bridge piers of varying geometrical complexity, ASCE J. Hydraulic Eng. **139**, 812 (2013).
[45] D. Nehari and F. Ballio, Three-dimensional analysis of the unidirectional oscillatory flow around a circular cylinder at low Keulegan–Carpenter and β numbers, J. Fluid Mech. **520**, 157 (2004).
[46] G. S. Constantinescu, H. Pasinato, Y. Q. Wang, J. R. Forsythe, and K. D. Squires, Numerical investigations of flow past a prolate spheroid, J. Fluids Eng. ASME **124**, 904 (2002).
[47] W. Y. Chang, G. Constantinescu, W. F. Tsai, and H. C. Lien, Coherent structures dynamics and sediment erosion mechanisms around an in-stream rectangular cylinder at low and moderate angles of attack, Water Resour. Res. **47**, W12532 (2011).
[48] W. Y. Chang, G. Constantinescu, and W. F. Tsai, On the flow and coherent structures generated by an array of rigid energed cylinders place in an open channel with flat and deformed bed, J. Fluid Mech. **831**, 1 (2017).
[49] W. Y. Chang, G. Constantinescu, and W. F. Tsai, Effect of array submergence on flow and coherent structures through and around a circular array of rigid vertical cylinders, Phys. Fluids **32**, 035110 (2020).
[50] M. Koken and G. Constantinescu, Flow structure inside and around a rectangular array of rigid, emerged cylinders located at the sidewall of an open channel, J. Fluid Mech. **910**, A2 (2020).
[51] P. Spalart, Detached eddy simulation, Annu. Rev. Fluid Mech. **41**, 181 (2009).
[52] D. C. Wilcox, *Turbulence Modeling in CFD*, 3rd ed. (DCW Industries, La Canada, CA, 2006).
[53] C. M. Rhie and W. L. Chow, Numerical study of the turbulent flow past an airfoil with trailing edge separation, AIAA J. **21**, 1525 (1983).
[54] J. Zeng, S. G. Constantinescu, and L. Weber, A 3D non-hydrostatic model to predict flow and sediment transport in loose-bed channel bends, IAHR J. Hydraulic Res. **46**, 356 (2008).
[55] J. C. R. Hunt, A. Wray, and P. Moin, Eddies, streams, and convergence zones in turbulent flows, studying turbulence using numerical simulation databases, Center for Turbulence Research Report CTR-S88, 193 (1988).